Application of Digital Image Correlation on the micro-scale of composites

Thesis

Dries Schroyen

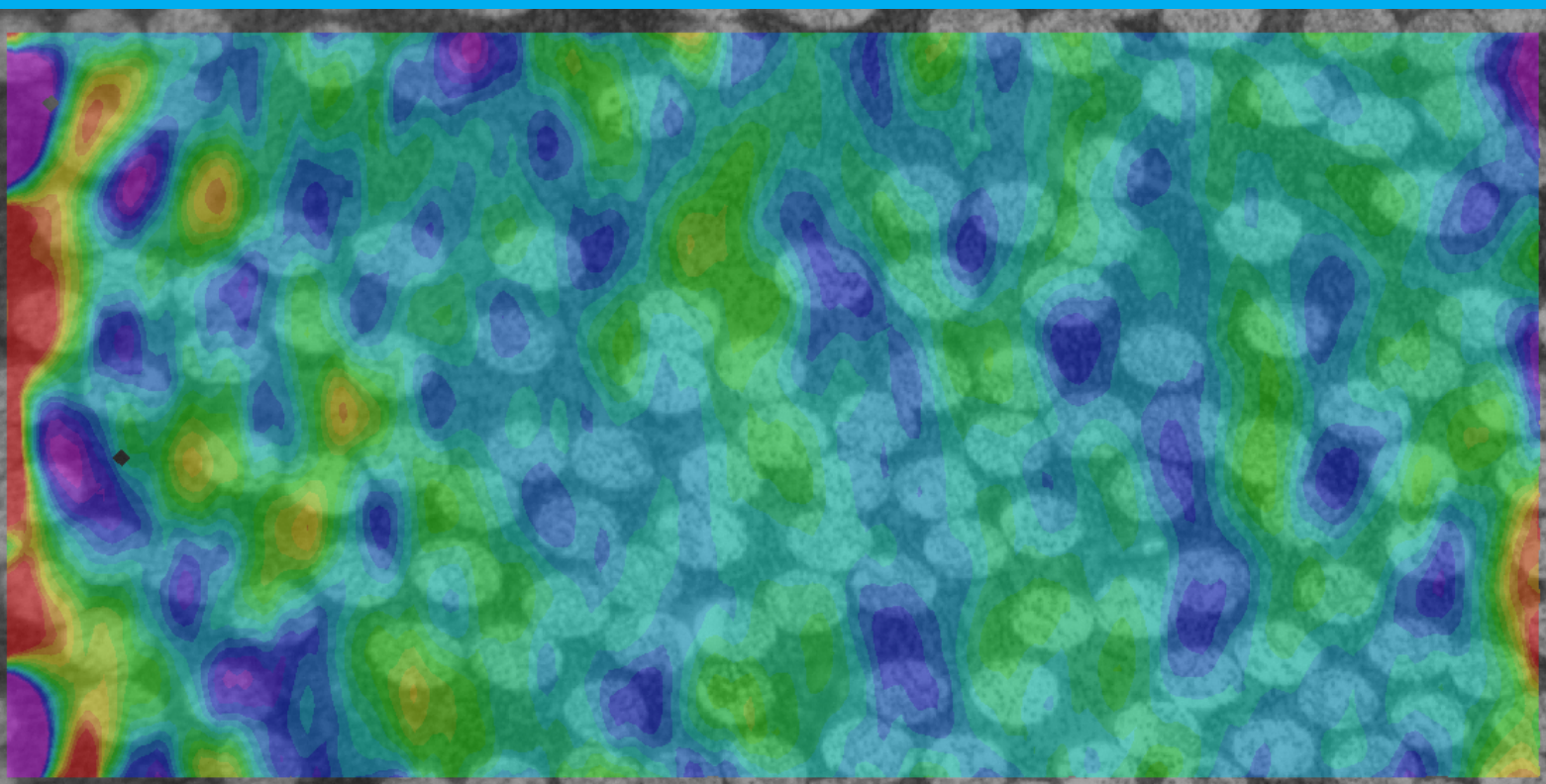

TU Delft

Application of Digital Image Correlation on the micro-scale of composites

Thesis

by

Dries Schroyen

to obtain the degree of Master of Science
at the Delft University of Technology,
to be defended publicly on Thursday September 20, 2018 at 1:00 PM.

Student number:	4214269	
Project duration:	March 1, 2017 – February 28, 2018	
Under supervision of:	Dr. A.G. Anisimov,	Delft University of Technology
	Dr. R.M. Groves,	Delft University of Technology
	Prof. dr. ir. W. Van Paepegem,	Ghent University
	Dr. D. Garoz Gómez,	Ghent University

An electronic version of this thesis is available at `http://repository.tudelft.nl/`.

TU Delft

Contents

1 Introduction

1.1. Thesis goal

During the last years, the use of fibre reinforced polymers, often called composites, has only increased. A composite is, by definition, a material consisting of two or more distinct components. With this combination, other, more desired properties than those of the individual constituents can be achieved. A broad range of materials falls under this definition of composite, from natural materials such as wood to man-made materials. These man-made composites have been around for a long time, as for example grass and straw has been used for centuries to reinforce clay. Nowadays, polymers are also reinforced with fibers, which are called fibre reinforced polymers [8]. When composite is used in the remainder of this report, it refers to this class of man-made composites, which can be carbon fibre reinforced polymer or glass fibre reinforced polymer, depending on the type of fiber reinforcing the polymer. During the last years, the use of fibre reinforced polymers, has only increased, not only in the aerospace industry, but also in automotive and wind energy industries. The reason for this is that a weight reduction is achievable using these materials [5].

The failure mechanics of composites are not yet fully known, and as such, more conservative safety factors have to be used in design. Creating knowledge of composite failure mechanisms will thus lead to lighter and safer designs. Mechanics of composites are more complex than traditional materials such as metals, because of the non-homogeneity of composite materials. Mechanics of composites are dominated by the properties of the fiber, the matrix and the fiber-matrix interface. The properties of the interface have a direct influence on delamination, cracking and other failure modes [1]. As a conclusion, it is important to study the micromechanical properties of composites, to understand the behavior of the composites on a larger length scale such as ply (millimeter) or part (meter) level.

Great advances in multiscale modeling have been made. At the smallest scale, the microscale, continuum mechanics can still be applied. The fibers and matrix are modeled as two different materials, with a fiber-matrix interface between them. These are modeled with Representative Volume Elements (RVEs), under different loading conditions, shown in Figure 1.1 on the left. However, experimental methods to validate the microscale models are not as well developed. Therefore, a lot of numerical simulations remain unvalidated [1]. There is thus a need for new experimental tools to validate simulations on the microscale, for RVEs up to tens of micrometers. This thesis project aims at providing such a tool.

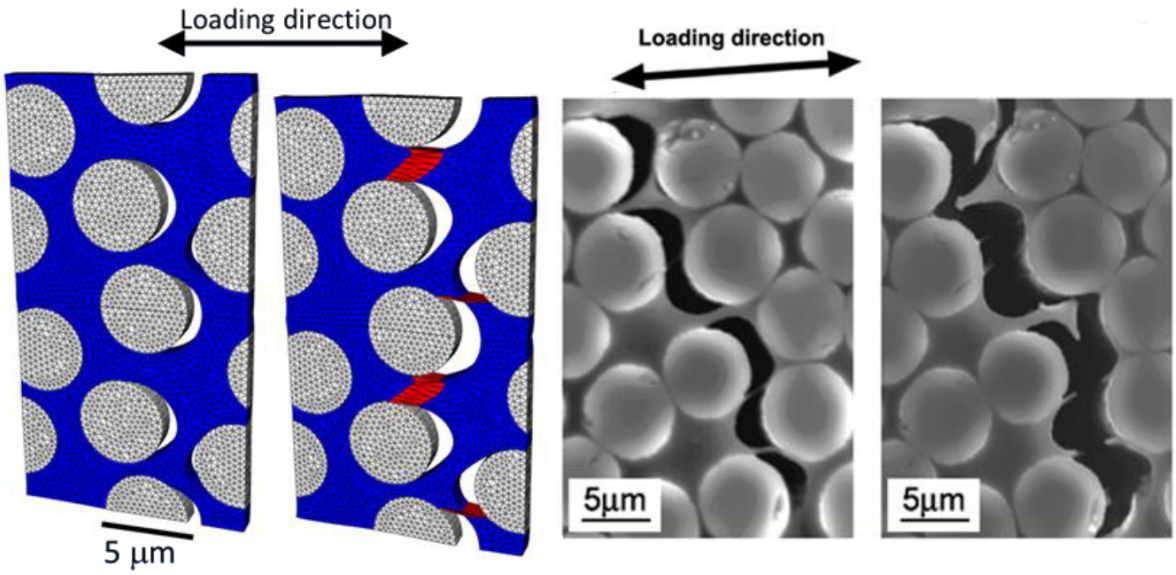

Figure 1.1: A Representative Volume Element (left) versus a Scanning Electron Microscopy image of a debonding composite [10].

A promising technique to determine full-field displacements and strains from digital images is DIC. As it is possible to make images of the composite (see Figure 1.1 on the right), DIC might be applied on them. The DIC technique was developed in the 1980's, and is already quite mature for structures in the millimeter to meter scale [36]. The challenge lies in applying this technique on the microscale on composite, which has only been done a few times before [4], [20], with a varying success. The particular challenges are all due to the small scale on which this technique will be applied. These are speckling of the specimen, loading the specimen and creating images of it. Furthermore, at this scale, the heterogeneity of the material is visible, imposing challenges for the DIC algorithm.

This project has been carried out as a master thesis in order to obtain the degree of Master of Science in Aerospace Engineering at the Delft University of Technology. As the research group of Mechanics of Materials and Structures at Ghent University has expertise in this field, the project has been carried out there. As such, this collaborative work is supervised from both universities during the 9 month project.

1.2. Research questions

The main research question was defined in the literature review [28] as: *Which system is needed to apply DIC on micro-scale testing of composites, in a reliable, verifiable and accurate (up to 10 nm) way with an optical microscope?* This accuracy is dictated by the current State of the Art accuracy of 17 nm with an optical system, elaborated on in Section 1.4. The aim in this project is thus to have an improvement in accuracy compared to the State of the Art.

This main research question has been split up into the following research questions. In the same way, these questions have been divided in multiple sub-questions:

1. What specimen preparation is needed, in relation to speckling, loading and imaging?

- Are additional surface treatments necessary?
- Which layup and specimen geometries are suitable?
- Which polishing sequence is sufficient?

2. Which speckle application method (with which parameters) creates a suitable speckle pattern?
   - Which method quantifies how good a speckle pattern is?
   - Which different methods exist for the application of speckles?
3. Which imaging system delivers images useful for DIC?
   - Which resolution is needed?
   - Which way will the system be calibrated?
   - Which Field of View (FOV) is needed to make results comparable with simulations?
4. Which algorithm comes up with reliable and accurate full field strains?
   - How do the DIC algorithm parameters influence the accuracy?
   - What influence has the heterogeneity of the composites on the results, and how can be coped with this? How does the shape of a subset influence results?

The final goal of the thesis is to answer all these questions, as the combination of these answers will answer the main research question.

1.3. Digital Image Correlation

DIC is not new. Already in 1983, Sutton et al. [30] developed an algorithm which traced subsets (smaller parts of an image) in a digital image. Later on, in 1986, Sutton et al.[31] showed that sub-pixel accuracy is achievable.

The working principle of DIC is rather simple. During deformation or movement of an object, a series of digital images is taken of it. Parts of these images (called subsets) are then tracked throughout the image sequence, as illustrated in Figure 1.2. When the displacement of each subset is known, the strains can be computed as well [36].

Since a single pixel is not unique, it is not traceable. Therefore, subsets are created. These are sets of pixels, which are distinguishable through the image series. The size of such a subset is an important parameter. If the subset is small, it becomes harder for the algorithm to trace, and image noise will have a stronger influence on the results. Larger subsets will remove this random influence, but they will also smooth out local information inside the subset. Another problem with large subsets is that the subsets can have a deformation which cannot be captured by the algorithm, such as quadratic or higher order deformations. This results in systematic errors, as described by Yaofeng et. al. [38]. Choosing the subset size is thus a trade-off between accuracy and localized information (resolution).
If an homogeneous displacement field is expected, subsets can thus be bigger, but if higher strain gradients are present, subsets have to be made smaller. A range for subset size is from 15 pixels and larger [36], but this is of course highly dependent for the problem at hand.

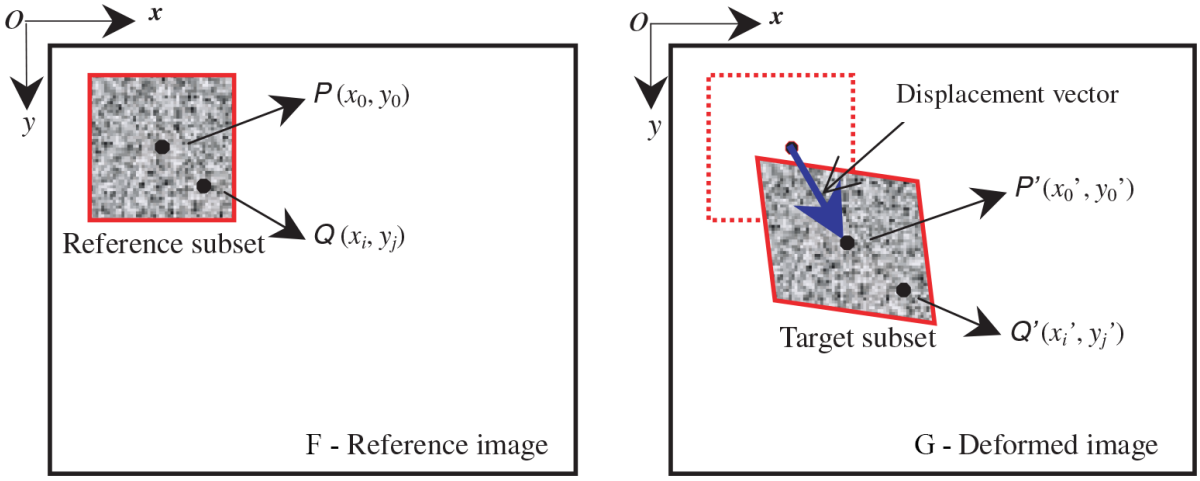

Figure 1.2: The working principle of DIC illustrated. [23]

To determine the motion of a subset, such as depicted in Figure 1.2, a correlation process such as that explained here is carried out. A function, called the Sum of Squared Differences, is set up, calculating the sum of squared differences in pixel intensity of the original image F and the deformed image G over the whole subset. The displacement $\bar{\mathbf{d}}_{\mathbf{opt}}$ for which this function is minimal, is the most likely displacement of the subset, as given by Equation 1.1 [36]. In this equation, $\bar{\mathbf{d}}$ is the vector describing the displacement of the subset, given by (dx, dy) in the case of Figure 1.3. The vector $\mathbf{x}$ is the position of the subset, given by (x_1, y_1) in the figure. The correlation can be done for every pixel (with a subset around it), but this is computationally costly. Therefore, a step size is defined in most software. This step size determines the spacing between pixels for which a subset is made (and a calculation done).

$$\bar{\mathbf{d}}_{\mathbf{opt}} = \text{argmin} \sum |G(\mathbf{x} + \bar{\mathbf{d}}) - F(\mathbf{x})|^2 \tag{1.1}$$

To perform the minimization in Equation 1.1, different approaches exist. One of the simplest is the Lucas-Kanade tracker [19], which uses a first-order Taylor expansion around the current displacement $\bar{\mathbf{d}}$ to iterate to the minimum. The approach described above currently only correlates subsets which stay in their original shape. However, this is rarely the case, since DIC is not only used to determine the motion of rigid bodies, but also to determine deformations. This causes the subsets to deform as well. To cope with this, the concept of subset shape functions is introduced. Further information and equations can be found in [36].

The Sum of Squared Differences can also be determined between discrete pixel values, which results in sub-pixel accuracy. To do so, the grey-values of the pixels have to be interpolated. Different methods exist for this, with the use of splines or polynomials being the most frequently used [27]. The use of this technique can result in an accuracy up to 0.01 pixel, which has been achieved with non-magnifying cameras [24]. For the application of DIC on micro-scale, this has not been reported yet.

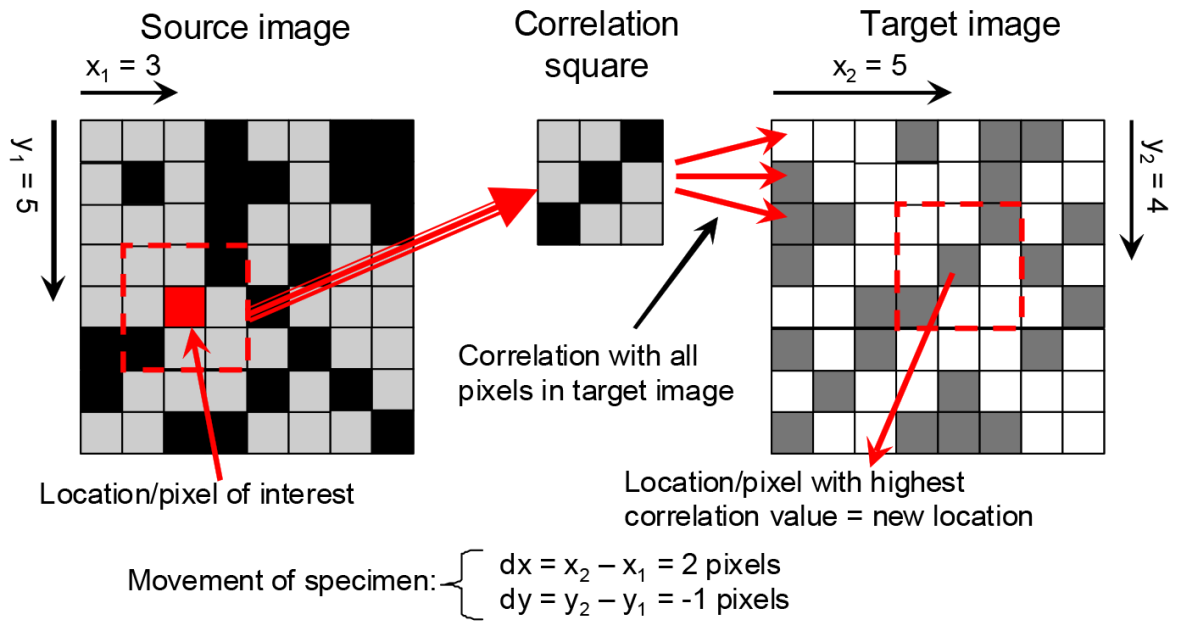

Figure 1.3: The correlation process. [16]

1.4. DIC on the microscale

The application of DIC on magnified images already started in 1990. Sutton et al. [32], developed a system to analyze surface deformations of magnified images with an optical microscope, magnifying up to 6 times. Nowadays, technology stands much further ahead and higher magnifications are possible. In this section, the current State of the Art is discussed.

Regarding optical microscopy images, currently the most accurate results have been achieved by Berfield et al. [2]. They used a Leica DM-R fluorescent microscope in combination with fluorescent rhodamine dye infused silica nanoparticles to create a speckle pattern. With this system, an image resolution of 134 nm/pixel was achieved while having a total field of view of 170 by 140 µm. With this system, a displacement accuracy of 17 nm was achieved. Although balancing on the edge of the possibilities of optical resolution, it still might be improved. This is one of the current challenges of the method of applying DIC to optical micrographs.

One way to improve the resolution is to switch to SEM. Because of the very different image creation principle compared to optical microscopy, other types of distortions arise. The resolution is not the challenge here, but modeling and correcting for these distortions is. Currently, a displacement accuracy of 1 nm has been achieved by Winiarski et al. [37].

With respect to the microscale of composites, DIC only has been applied on SEM images, by a few researchers. Canal et al. [4] were the first to apply DIC on the microscale of composites to analyze the micro-mechanical behavior between fibers and matrix. This was done using SEM images, with magnifications from 250x to 2000x and 6000x. At the lowest magnification of 250x, interactions between fiber and matrix were not observed, since they are completely smoothed out over the subsets in the DIC algorithm. At the higher magnifications, a speckle pattern was applied using alumina particles. After applying uniaxial compression perpendicular to the fibers using a micro-electro-mechanical testing device, strains were observed to be different between the stiffer fibers and less stiff matrix. Particularly, high strain concentrations were found in matrices between fibers aligned in the loading direction. This was in accordance with Finite Elements Modeling (FEM) simulations of the observed area. However, due to the averaging effect of the subsets, sharp strain gradients at the fiber-matrix interface were smoothed out, as is visible in Figure 1.4.

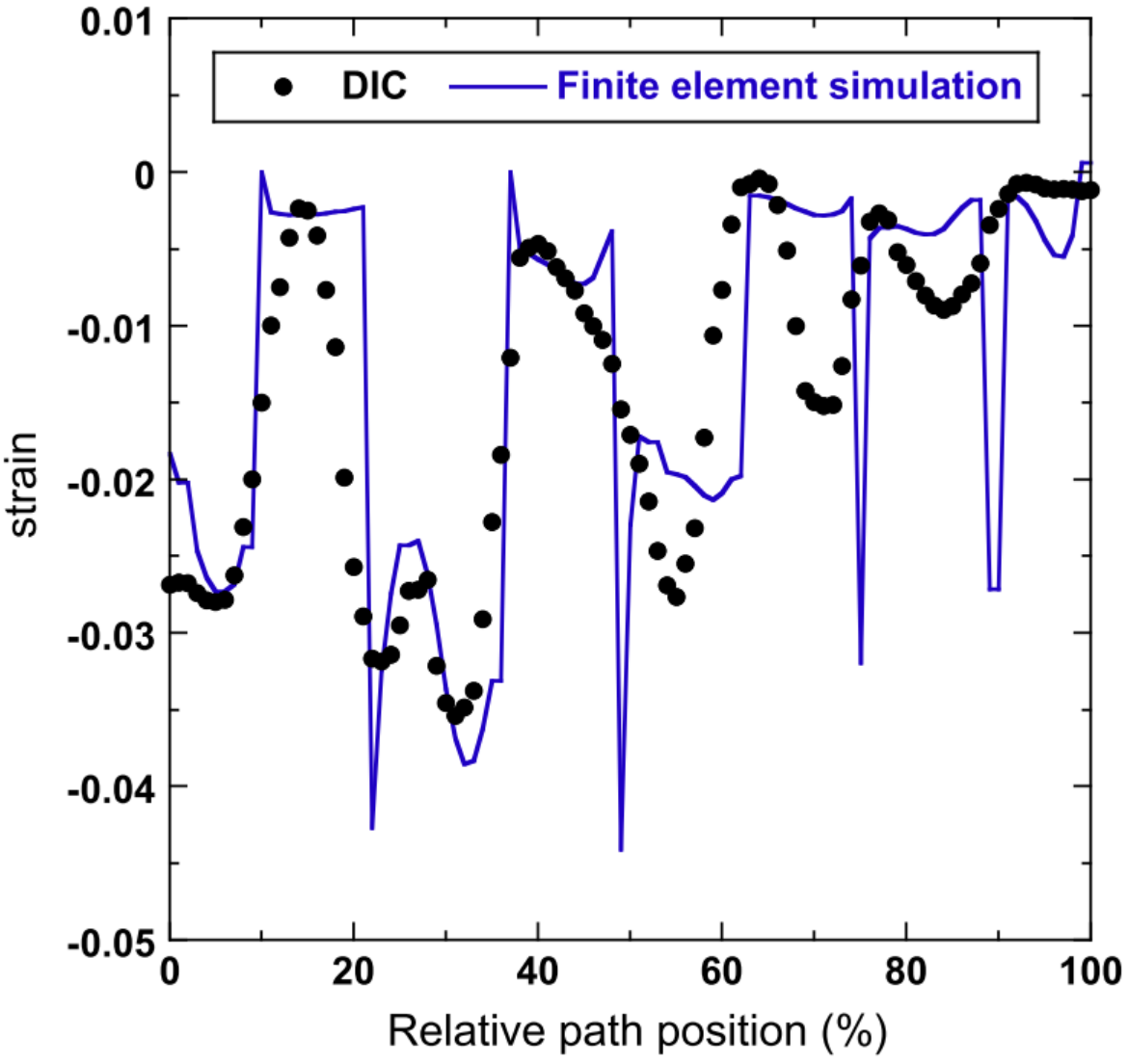

Figure 1.4: Comparison of DIC measurement and FEM simulation along a line through the region of interest. Note that the two coincide quite well, but that the DIC measurements are smoothed out. [4]

Mehdikhani et al. [20] applied DIC on SEM images of composites as well. Using alumina powder, with particles of 220 nm average size, a speckle pattern was created. They split the errors of the method into 2 categories: the measurement errors, due to the DIC algorithm; and the microscopy errors, due to the SEM imaging. To quantify the measurement error, a method called *strain deviation analysis* was applied. A micrograph of the region of interest was virtually elongated in one direction by an algorithm that deforms the image, and the DIC algorithm was run on it. The virtual strain applied on the image should be in the order of magnitude of the expected strain in the test to make this method a reasonable estimate for the measurement error [20]. Ideally, applying this virtual strain should result in a homogeneous strain field, but due to the algorithm, the strain is not uniform. The standard deviation of the strain field was calculated, and this is a way to quantize the measurement error. To investigate the microscopy error, 4 rigid-body micrographs were taken while the specimen is not loaded, with a 30s interval. DIC was used to analyze them, ideally resulting in zero strain. Strains deviating from zero were found, giving an indication of the microscopy error. After images from the deformation are acquired and analyzed with DIC, the values for the errors were compared with the measurements. The maximum measurement error strain was 0.0008 and the maximal microscopy error strain was 0.0005, while the maximum strain in the real deformation map was 0.0050. Since both types of errors were small in comparison to the strains occurring in the test, they were assumed to be negligible. To reduce noise in the measurements, linear regression was performed during the linear loading stage. This limited the method to be useful in the linear region only, so damage initiation and propagation could not be studied this way. However, a better method to cope with microscopy errors and a specialized algorithm for heterogeneous materials is needed to improve the method further.

In the same study [20], to compare measurements with simulations, a model was constructed based on the geometry of the region of interest. Then, DIC measurements of the edges of the region of interest were used as boundary conditions for the edges of the model. Finally, the strain field of the model and the DIC measurement were compared, as shown in Figure 1.5.

In later work of Mehdikhani et al. [21], the same method was used to check for measurement and microscopy error, and no corrections were applied either. The measurement error was estimated to be below 5 nm in this work, but no quantitative information about the microscopy error was provided.

1.5. Accuracy definition

Using DIC, displacements of subsets can be determined, and from these displacements, strains can be calculated. As defined in Section 1.2, the accuracy goal is 10 nm, as this is an improvement from the current State of the Art.

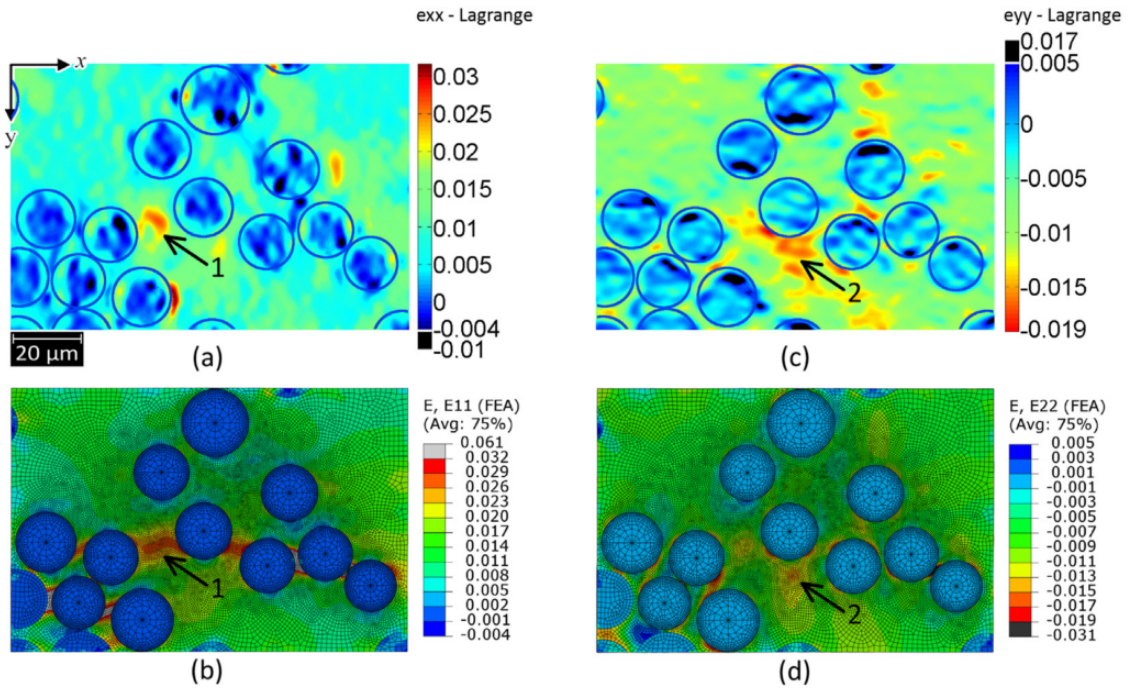

Figure 1.5: Comparison of strain fields: DIC measurements (a: ϵ_{xx} (strain in x-direction), c: ϵ_{xx}) and FEM simulation (b: ϵ_{yy}, d: ϵ_{yy} (strain in y-direction)). Strain concentrations found in both strain fields are indicated with arrows. [20]

When only rigid body motion is applied to the specimen, the displacement of each subset should be equal. This is also true for stationary images, which however can be influenced by vibrations, causing a rigid body motion. To determine the accuracy of displacement, the assumption is made that the average displacement of the subsets (in both directions), is the true overall displacement due to rigid body translations. The difference between the mean displacement and the actual displacement of a subset is then due to the inaccuracy of the method. As displacements are determined in 2 directions, the total inaccuracy displacement is determined using Pythagoras' theorem. To define the accuracy, it is possible to determine the standard deviation from this inaccuracy displacement value as a measure of accuracy. This leads to a definition that is only dependent on one DIC parameter, namely the subset size. Furthermore, using this method will give an answer to the research question *"Which system is needed to apply DIC on micro-scale testing of composites, in a reliable, verifiable and accurate (up to 10 nm) way with an optical microscope?"*. If the distribution of the subset displacements is assumed to be a normal (or Gaussian) distribution, accuracy can be defined with confidence intervals and the standard deviation. Finally, the convention is made that the accuracy is defined within the 95% confidence margin, corresponding to twice the standard deviation of the inaccuracy displacements.

Equivalently, if only rigid body motion is present, the strain at each subset should be zero. Again, taking a standard deviation of the strain could be taken as a measure of accuracy. The advantage here is that this accuracy is expressed in terms of strain, which makes it easier to asses whether the accuracy is sufficient to compare to simulations. The drawback is that this measure is dependent on 3 DIC parameters, being the subset size, step size and filter size. This makes results harder to compare, as for example taking a smaller step size immediately leads to higher false strains. Nevertheless, this method has been used as well throughout the project, in which cases the 3 parameters (subset size, step size and filter size) have been kept equal to make results comparable.

1.6. Conclusion

The goal of this thesis project is to provide a tool which can be used to apply DIC on the microscale of composites. This creates the opportunity to perform full field measurements on this scale, which are valuable to validate RVE simulations, which in turn creates more knowledge in composite mechanics. A research question has been defined and based on literature research, an accuracy goal of 10 nm has been set. The best accuracy found in literature while using an optical microscope is 17nm, achieved by Berfield et. al. [2]. The technique of DIC on larger scales than the microscale is mature. On the microscale, a lot of research is still going on, as well as on applying DIC on optical microscopy as on SEM images. Finally, a method to determine the accuracy of the subset displacement calculation is set up. This accuracy will be determined using images of undeformed specimens, where the spread of the subset displacements (measured by the standard deviation) will provide the measure of accuracy.

2

Specimen preparation for microscopy and speckling

In this Chapter, the preparation of the specimens is discussed. The 2 materials used are carbon fiber composite (Section 2.1) and glass fiber composite (Section 2.2). These are the 2 most commonly used composites, on which most composite research is focused. Furthermore, to determine surface properties, contact angle measurements were performed in Section 2.3, and to improve these properties, surface treatment by plasma is examined in Section 2.4. Finally, a conclusion is drawn in Section 2.5.

2.1. Carbon fiber specimens

The carbon fiber composite used in this project was produced by Mitsubishi Rayon Co.,Ltd. As fiber, the PYROFIL™TR 50S15L is used. This is a standard modulus carbon fiber with high tensile strength. It is produced as a continuous fiber with 15000 filaments with an average fiber diameter of 6.8 µm. The tensile modulus of the fibers is 240 GPa and the maximal elongation 2% before failure. As resin, PYROFIL™#360 is used. This is an epoxy resin, usually cured at 130 °C, with quick curability and good heat resistance. A small amount of black pigment is added to color it black, for aesthetic reasons. These two constituents are used to create the PYROFIL™Unidirectional Composite. This is done using a compression molding process. This gives a composite with a resin content of 30 wt%.

To prepare the composite for optical microscopy, small samples (of 15 by 25 mm) were cut from the laminate. This was done using a water-cooled diamond saw. The side with a cut perpendicular to the fibers was polished. Before automatic polishing, the specimen is embedded in epoxy. For this, EpoxiCure™2 Epoxy Resin was mixed with EpoxiCure™2 Epoxy Hardener, with a weight ratio of 100:23. Composite samples were placed in a Fixiform 1.25 inch cylindrical mold, and the epoxy was added to it. After a curing time of minimum 6 hours, the specimens can be taken out of the mold and were ready to polish. This results in cylindrical specimens as shown in Figure 2.1. The drawback of this method is that, due to the embedding process, applying a load to the round specimens is difficult. If loading is to be added to the specimen, the same polishing procedure can be used with flat specimens in a clamping device.

Table 2.1: The polishing sequence for carbon fiber on the Struers Tegramin-30 automatic polishing machine.

Step	Surface	Suspension/Lubricant	Time [min]
1	Piano 220	Water	1,5
2	Piano 600	Water	6
3	Piano 1200	Water	6
4	SiC-Paper #2000	Water	11
5	SiC-Paper #4000	Water	6
6	Mol	DiaPro Mol, 3 µm	1,5
7	Nap	DiaPro Nap R, 1 µm	1,5

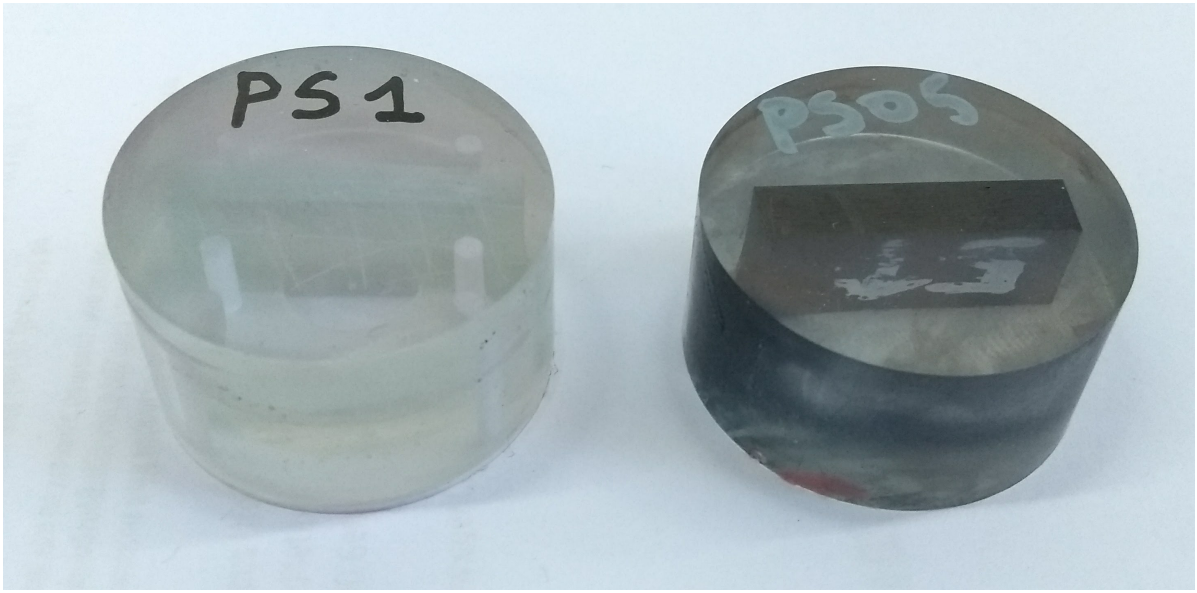

Figure 2.1: Image of an embedded, polished glass fiber (left) and carbon fiber (right) composite.

When the specimens are embedded, the automatic polishing can start. This was done with a Struers Tegramin-30 automatic polishing machine. All grinding and polishing surfaces, as well as polishing suspensions, were also from Struers. These were the DiaPro Mol and DiaPro Nap, which were diamond suspensions in oil, with diamond particles of respectively 3 and 1 µm. The different grinding and polishing steps used, developed by Mechanics of Materials and Structures department of Ghent University, are summarized in Table 2.1. Intermediate and final images are given in Figure 2.2. These images were made with a Keyence VHX-2000 digital microscope, on which is elaborated in Chapter 4.

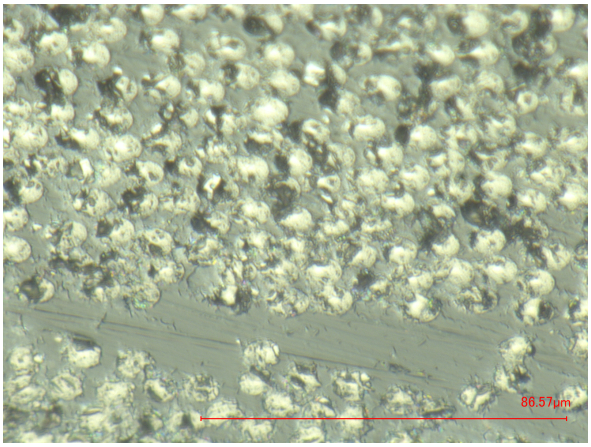

(a) Specimen surface after step 4.

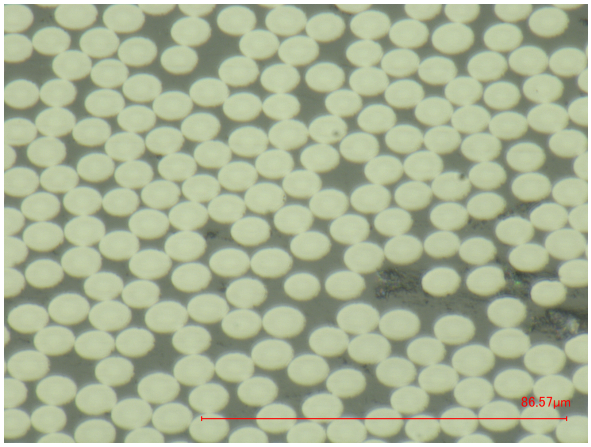

(b) Specimen surface after last polishing step.

Figure 2.2: Microscopic images between polishing steps and final result (Keyence VHX-2000 (see Chapter 4) at magnification 2500x).

2.2. Glass fiber specimens

For the glass fiber composite, the manufacturing was done in the composites lab of the Mechanics of Materials and Structures department of Ghent University.

As fibers, unidirectional E-glass from the UDO®line of SGL Group were used. Using resin transfer molding, the unidirectional glass fibers were infused with the EPIKOTE™Resin MGS®RIMR 135 epoxy, mixed with the EPIKURE™Curing Agent MGS®RIMH 134 hardener (mixing weight ratio 100:30). This process was done at room temperature (25°C). Sample preparation was similar to the carbon fiber specimens, as far as cutting and embedding goes. The polishing process was different, and summarized in Table 2.2. A microscopic image of the polishing is given in Figure 2.3. Despite the fact that this polishing cycle already has been optimized, broken off fibers are still visible as black parts of fibers.

Table 2.2: The polishing steps for glass fiber.

Step	Surface	Suspension/Lubricant	Time [min]
1	Piano 220	Water	2,5
2	Piano 600	Water	2,5
3	Piano 1200	Water	2,5
4	SiC-Paper #2000	Water	2
5	SiC-Paper #4000	Water	2
6	Mol	DiaPro Mol, 3 µm	1
7	Nap	DiaPro Nap R, 1 µm	1

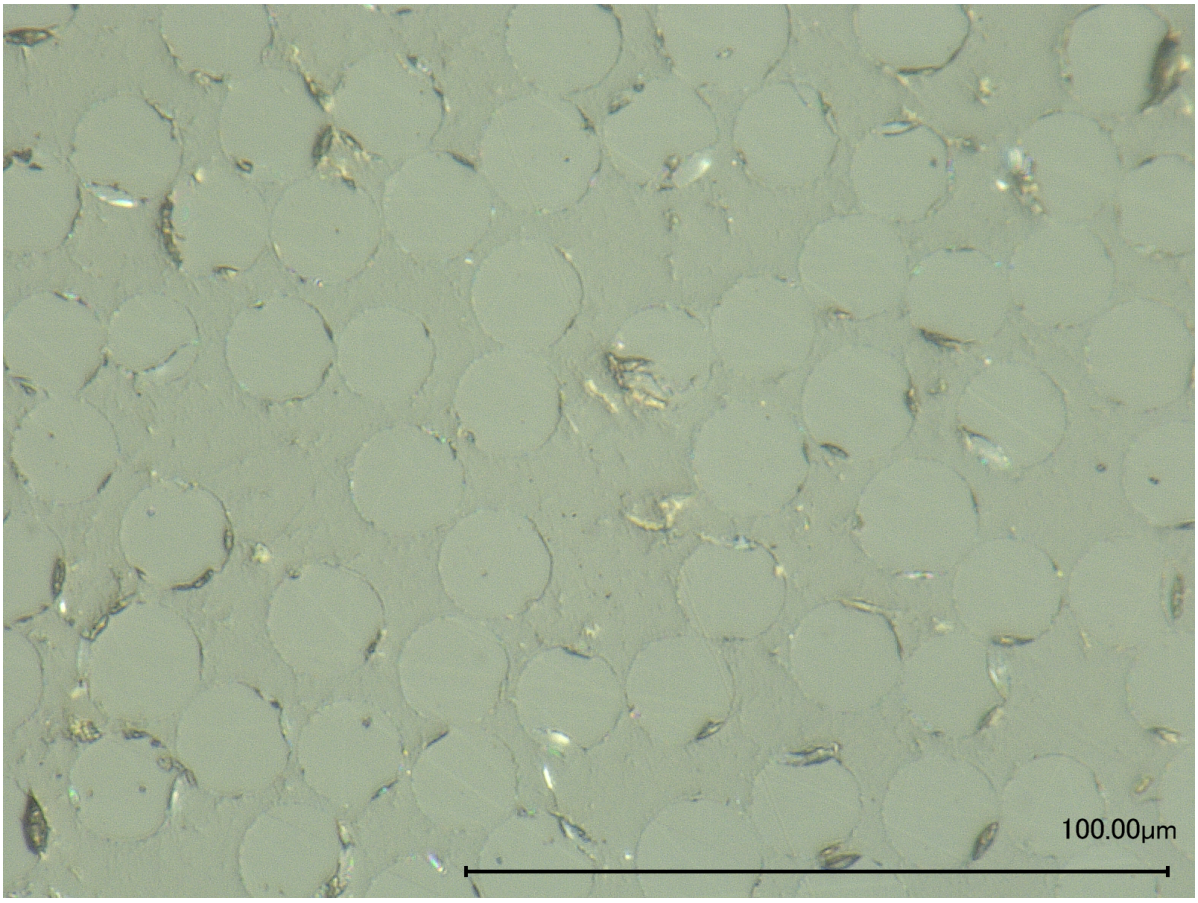

Figure 2.3: Microscopic image of the polishing result (Keyence VHX-2000 at magnification 2000x).

Even though the polishing sequence was not perfect, it was deemed sufficient to continue. The main reasons were that fibers were clearly distinguishable, and defects on fibers were never bigger than a quarter of a fiber. Furthermore, using the automatic polishing procedure, the process is repeatable.

2.3. Contact angle measurements

As will be clear in Chapter 3, the behavior of drops on the specimen surface is important. Therefore, contact angle measurements of the polished carbon fiber and glass fiber composites were performed. With this, the wettability of a liquid on this surface was measured. A simple drop test was performed by following procedure:

1. Dropping a liquid on the polished surface with a pipette
2. Taking an image with a Dinolite USB microscope
3. Measuring the angle with Photoshop©(see Figure 2.4)

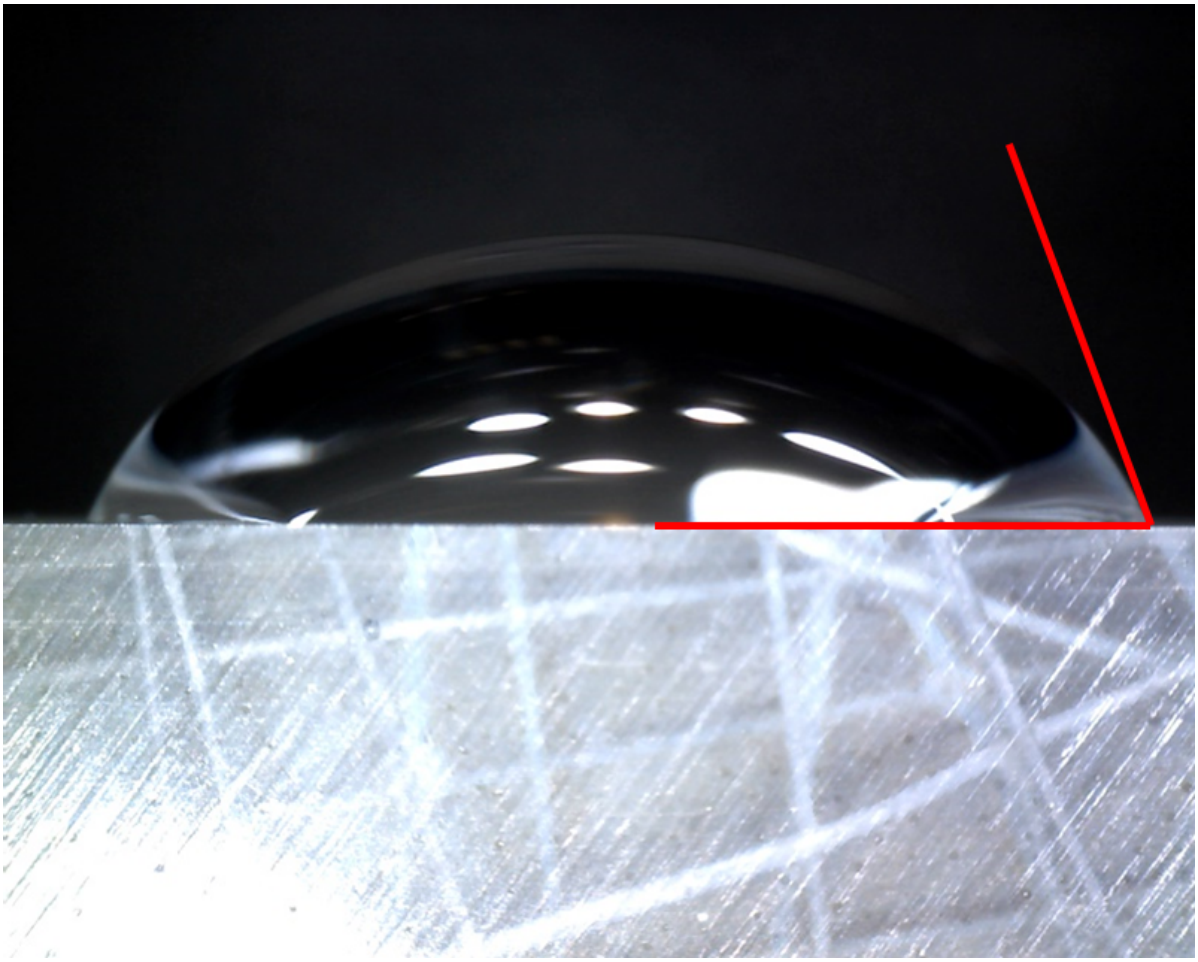

Figure 2.4: Image of the drop for the contact angle measurement. Imaged by Dinolite, and angle drawn and measured in Photoshop.

This procedure was carried out 10 times for each material. Results of these measurements (mean value and standard deviation) are displayed in Table 2.3. Between carbon or glass fiber composite, there is only a small difference of 3.6°. However, between the liquids is a large difference. Demineralized water does form a drop, whereas none of the solvents do. Solvents used were acetone, methanol, ethanol and isopropanol.

Table 2.3: Results of the contact angle measurements

	Carbon Fiber	Glass Fiber
Demineralized water	72.2°(σ=8.2°)	68.6°(σ=3.8°)
Solvents: acetone, methanol, ethanol, isopropanol	0°(complete wetting)	

2.4. Plasma treatment

To improve the surface wetting (discussed in Section 2.3), the surface energy should be altered. This can be done with mechanical, chemical or energetic processes. As mechanical processes such as grit blasting and abrasion will visibly alter the polished surface, these are not useful. Chemical processes such as solvent cleaning were already performed after polishing, so this will not improve any further. As chemical process, etching or anodising are possible, but not tried since they are aggressive to the composite material, especially the polymer matrix. The last category, energetic processes, include plasma treatment, corona discharge and flame treatment. To try out energetic processes, plasma treatment was chosen, since it is readily available in the Mechanics of Materials lab of Ghent University.

By bombarding the surface with plasma, the surface energy changes. This was done with a Fischione M1020 plasma cleaner, using Argon gas and and energy of 15 eV. Normally, for plasma cleaning, times around 10 minutes are advised [11]. This was tried on the two different types of composites, and after the treatment full wetting (contact angle of 0°) with water was achieved. When looking closer to the surface in Figure 2.5, a severe problem can be noted. The plasma treatment leads to the matrix deteriorating strongly. After 10 minutes, the matrix of the carbon fiber has been taken away by 15 µm (see Figure 2.5c), and the matrix of the glass fiber composite by 20 µm (see Figure 2.5d). If this process is assumed to happen linearly, 0.5 µm would already be taken away in 20 seconds, making it impossible to focus, since the depth of field of the optical microscope is limited (see Chapter 4. Because of this effect, the whole image cannot be in focus at once, and a special depth composition can be made to create a clear image. This process would cause problems for the DIC algorithm, since the images made with this technique are a composition of images at different focus, leading to bad DIC results. Furthermore, fibers sticking out could also change mechanical properties, making it uncomparable to simulations. However, the fibers sticking out toothbrush-like (seen in Figure 2.5a and 2.5b) can explain why complete wetting occurs, as through capillary action, the water is spread over the whole surface. Finally, it can be concluded that plasma treatment is not a good surface treatment for the purpose of this project.

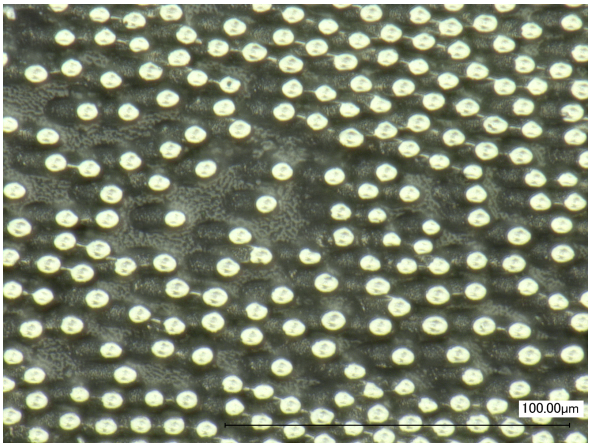

(a) Carbon fiber specimen surface, depth-up image reconstruction (Keyence VHX-2000 at magnification 2000x).

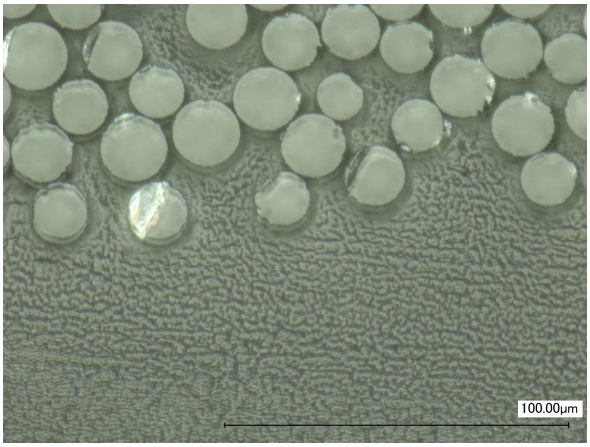

(b) Glass fiber specimen surface, depth-up image reconstruction (Keyence VHX-2000 at magnification 2000x).

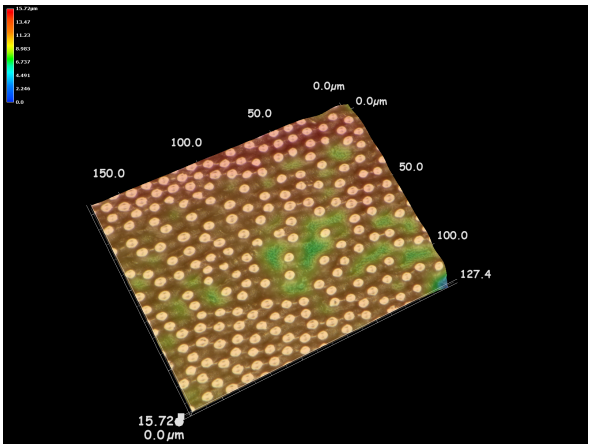

(c) Carbon fiber specimen surface, 3D reconstruction (Keyence VHX-2000 at magnification 2000x).

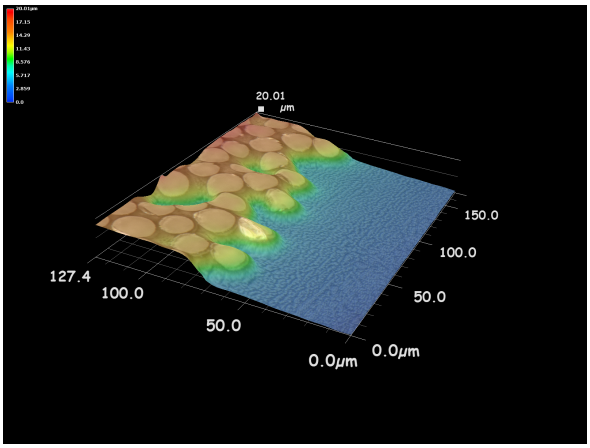

(d) Glass fiber specimen surface, 3D reconstruction (Keyence VHX-2000 at magnification 2000x).

Figure 2.5: Specimen surfaces after 10 minutes plasma treatment. Images by Keyence VHX-2000 (see Chapter 4)

2.5. Conclusion

The preparation of the specimens is defined. After production of unidirectional fiber composites by infusion with epoxy resin, specimens of 15 by 25 mm were cut from the laminate with a diamond saw. On the 25mm side, which is perpendicular to the unidirectional fibers, polishing was performed. The polishing sequence is different for each composite. To ensure a good, repeatable polishing process, automated polishing was used. Therefore, specimens were embedded in a resin. If embedding is not possible, it is possible to use a clamping device for specimens to put them in the automatic polishing machine. Contact angle measurements were performed, which showed that water did not completely wet the surface, the solvents do. A surface treatment (plasma treatment) has been examined, but was found to be detrimental to the surface.

3

Speckle application

As the mechanics between fiber and matrix are of primary interest, it is wise to take subsets not larger than half a fiber. The smallest fibers are the carbon fibers, with a diameter of 6.8 µm. This would result in subsets of around 3.4 µm. For good correlation, a rule of thumb is that each subset should contain at least 3 speckles in each direction [36]. In the ultimate case of touching speckles, the maximum size is 1.1 µm. Speckles smaller than this size are thus needed. To determine the best speckle application method, it is first determined with which criteria the method has to comply in Section 3.1. Two types of methods are discussed, which are template patterning in Section 3.2 and nanoparticle patterning in Section 3.3. These methods are compared in Section 3.4. Finally, the parameters of the best method are optimized in Section 3.5.

Depositing nanoparticles on substrates is an inexpensive and fast technique, covering a whole sample at once. It is suitable for a wide range of specimens, either metallic or non-metallic, and from flat to curved specimens [15]. Another advantage is that the size of the speckles is easily controllable by the size of nanoparticles used. Different types of nanoparticles can be used, such as metallic particles (gold [15] or aluminum [21]) or silica nanospheres [2]. Furthermore, yttria-stabilized zirconia particles have been used as well [37].

Template patterning is a speckling method that has been used before by Kammers et al. [13]. By placing a mask on a specimen, sputtering it with a thin metal layer and removing the mask, a pattern is created.

Another method to apply a speckle pattern on this scale is the use of electron beam lithography, which is a technique classically used in producing micro-electronics. With a SEM beam and the use of etching, a predefined pattern can be applied on the substrate [9]. This has the big advantage that a predefined pattern can be applied on the specimen, but comes at the cost of having to use expensive equipment. With the Focused Ion Beam (FIB) technique, milling or depositing material on the micro-scale is possible. The milling works by accelerating Gallium ions to a specific site [17]. The deposition at the other hand, works with a precursor gas in the chamber of a dual-beam microscope. When the ion beam bombards the gas, it is decomposed into volatile and non-volatile parts [39]. The non-volatile parts stay on the surface, forming the speckle pattern. As with the electron beam lithography, this process is expensive, but provides the advantage that a predefined pattern can be applied. Since these 2 methods involve complex equipment, they are not examined during the project.

3.1. Quality assessment

First of all, a speckle pattern has to be random (without repetitive patterns), isotropic and with a high contrast to ensure good correlation [36]. Different methods to apply such a speckle on this scale are explored, as explained in Sections 3.2 and 3.3.

To determine which speckle application method is best suitable, every method is held against some quality criteria. These are:

Distribution The speckles have to be uniformly distributed across the surface, with everywhere the same density. As mentioned before, they have to be random and isotropically distributed.

Repeatability Repeating the process should produce the same results. For this, manual actions have to be minimal.

Ease of use The process should be easy to execute, preferably by 1 person, without supervision, and without specialized equipment.

Furthermore, the density of the speckle pattern is very important for correlation. This is depending on parameters of the application method, and not on the method itself. Therefore, a suitable method is chosen based on the three quality criteria listed above. Later, this method is optimized, as described in Section 3.5 to come to the best speckle application method.

3.2. Template patterning by sputtering

The principle of template patterning has been considered because the principle is simple and easy to repeat. A template, mostly filter, is placed on top of a specimen as a mask. Then, metal is sputtered on top of it. Part of the metal stays on top of the filter, and some of it penetrates through the pores, creating a speckle. When the mask is removed, only the speckle remains.

The sputtering is done by magnetron sputtering, a physical vapor deposition process in a vacuum chamber. This is a magnetically assisted gas discharge process, which uses ion bombardment to evaporate metal from a target. The gas-phase metal is transported to the substrate and condensates [6]. In the particular setup used (at Campus de Sterre of Ghent University), typical process parameters are used, but the distance between target and substrate is kept relatively high to decrease the heat load towards the masks [6]. The process parameters used are:

Target metal Constantan (Cu55Ni45)

Distance target - substrate 10 cm

Cathode current 0.3 A

Argon pressure 1.2 Pa

As mask, 2 types of materials are used. The first one is simple filter paper, and the other types are electro-spun nanofibres [8]. The exact mask materials are:

1 Schleicher & Schuell 595 filter, thickness 150µm, pore size 4-7µm

2 Electro-spun, heat-treated silica nanofibre veil [8]

3 & 4 PA6.9 (Polyamide 6.9) nanofibre veil [8]

To ensure the masks adhere well to the substrate, a drop of isopropanol was put on the surface before applying the filter on it. This pulls the filter to the surface. Without this process, speckles can be blurry [13].

Figure 3.1: The specimens before magneto sputtering, with mask (except for specimen 4).

Microscopic images of the speckle pattern are shown in Figure 3.2. In Figure 3.2a and 3.2b, it can be seen that the speckling density is not sufficient. This is due to the high aspect ratio of the filter, which is the ratio of filter thickness to pore size. If this is too large, the metal does not penetrate the filter very well. This could be solved by repeating the process multiple times[13]. However, with such a low speckle density, this would take a lot of time. The distribution of the speckles is also a problem, since the speckles are more attracted to the fibers than to the matrix. The repeatability of the process is good, because the process is machine-controlled, and no manual handling is required during sputtering. However, the ease of use is not because complex equipment is needed. Furthermore, when using silica nanofiber veils as mask, the fibers tend to break and stick to the surface after sputtering, as seen in Figure 3.2c and 3.2d. In the images of specimen 3 (Figure 3.2e and 3.2f), with the PA6.9 nanofiber veil, the speckles are quite small, which would make a finer correlation possible. However, the contrast with the glass fiber specimen is bad. Note: the black dots in Figure 3.2e are not the applied speckles, but edges of the glass fibers which broke off, as seen more clearly in Figure 3.2f.

3.3. Nanoparticle patterning

The second type of application method uses nanoparticles. By placing a layer of them on the surface of a specimen, a pattern is created. Two types of nanoparticles are used. The first is Aerosil R972 (manufactured by Evonik), which is hydrophobic fumed silica. This forms aggregates with a size of 200 nm. Upon setting, these can agglomerate further to a bigger network, which can create a pattern. The second type are polystyrene microspheres, manufactured by Spherotech and delivered as a dispersion in demineralized water. 3 sizes are used, the 1 µm (range 1.0-1.4 µm), the 500 nm (range 400-600 nm) and the 100 nm (range 100-200 nm). To apply these nanoparticles on the specimens, 4 different application methods are discussed in following subsections.

3.3.1. Drop deposition

Drop deposition is an easy and very straightforward procedure to deposit the nanoparticles. A dispersion of the nanoparticles in made in a demineralized water, after which a drop of it is placed on the specimen en let to dry. For the polystyrene nanospheres of 500 nm, different solutions are prepared. With a fine pipette, 2 drops of the manufacturer's dispersion are diluted with 1ml of demineralized water. Solutions thus used started with 2 drops/ml, were further diluted down to 1 drop/ml, 0.5 drop/ml and 0.25 drop/ml. Results of the 0.5 drop/ml are shown in Figure 3.3, but are similar for all concentrations.

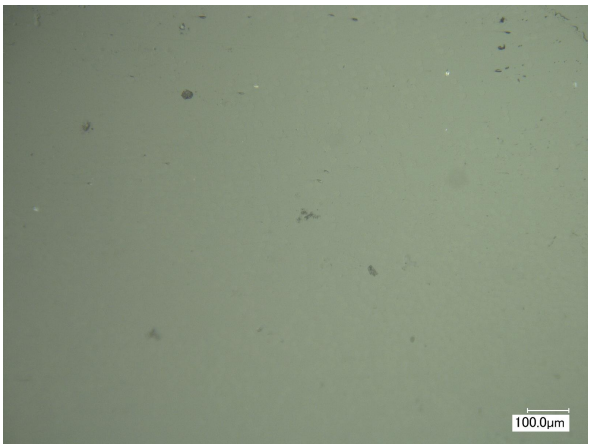

(a) Specimen 1, Keyence VHX-2000 at magnification 250x

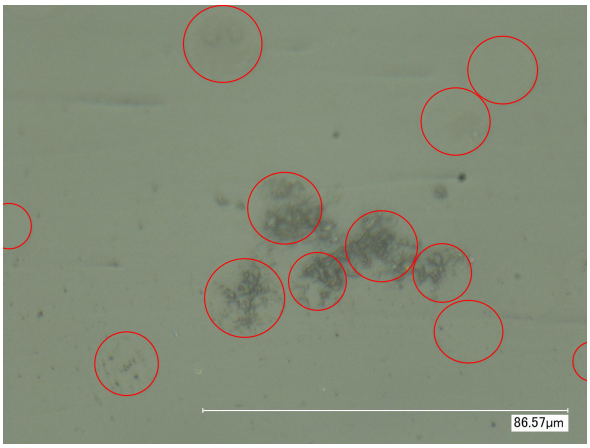

(b) Specimen 1, Keyence VHX-2000 at magnification 2500x. Fiber edges marked in red.

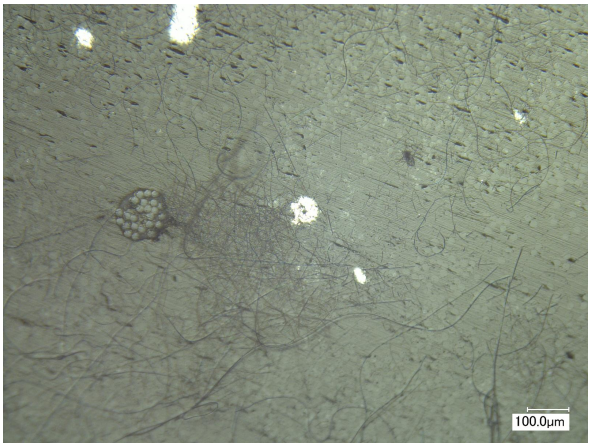

(c) Specimen 2, Keyence VHX-2000 at magnification 250x

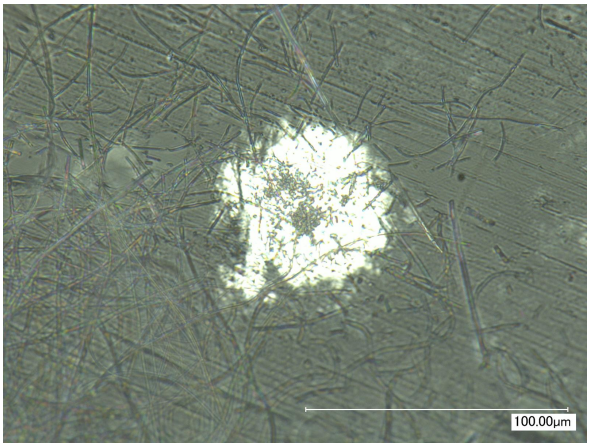

(d) Specimen 2, Keyence VHX-2000 at magnification 1500x

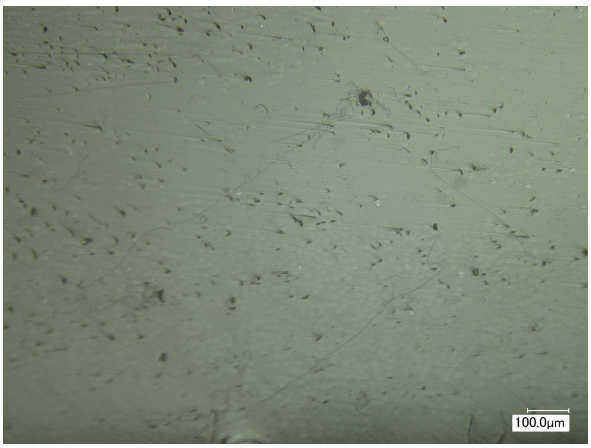

(e) Specimen 3, Keyence VHX-2000 at magnification 250x

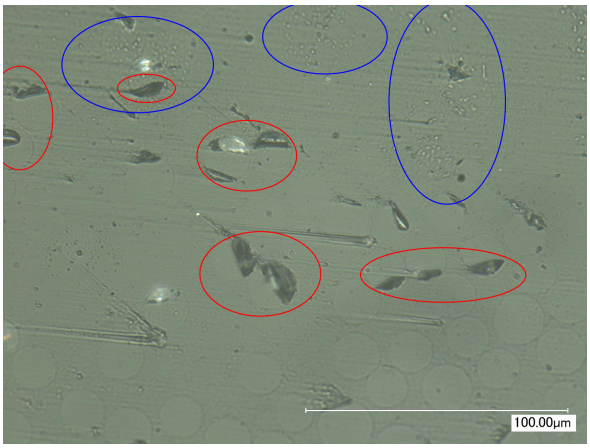

(f) Specimen 3, Keyence VHX-2000 at magnification 1500x. Groups of speckles indicated in blue, broken off fibers in red.

Figure 3.2: Microscopic images of the speckle pattern after sputtering

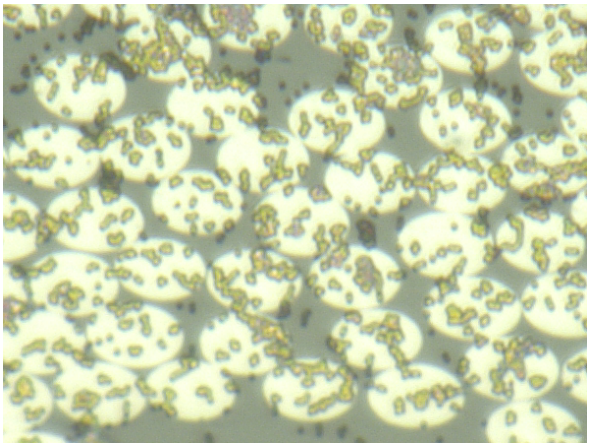

(a) High magnification (2000x) of a good region, taken by Keyence VHX-2000.

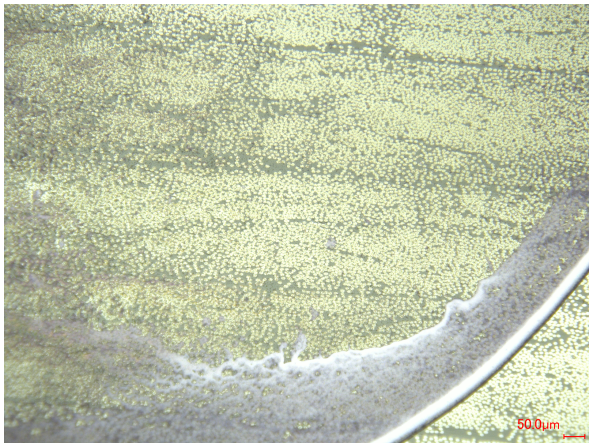

(b) Low magnification (250x), taken by Keyence VHX-2000.

Figure 3.3: Results of drop deposition of 500 nm polystyrene spheres (0.5 drop/ml) on carbon fiber composite

As can be seen in Figure 3.3a, this yields quite good results in some areas. However, the distribution of the particles is not uniform at all. At the edge of the drop, many more particles are present after the drop has dried. This is due to the so-called coffee ring effect (clearly visible in Figure 3.3b). The repeatability of the process is average, since it involves placing the droplet manually, but this is a simple procedure. The ease of use is very high, since no special equipment is needed.

3.3.2. Dip-coating

The preparation for dip-coating is the same as for the drop deposition: the polystyrene dispersion is diluted with demineralized water. For the dipcoating, a concentration of 4 drops/ml is made, again measured with a fine pipette. The Aerosil R972 is delivered as a powder. Since it is hydrophobic, it is dispersed in isopropanol (1 spoon in 4ml). The solutions are shaken and put in a Petri dish, after which the specimens are dipped in it by hand.

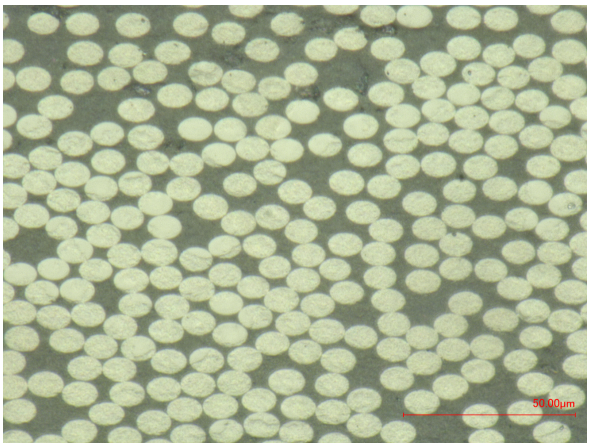

(a) Aerosil dipcoating (Keyence VHX-2000 at magnification 2000x)

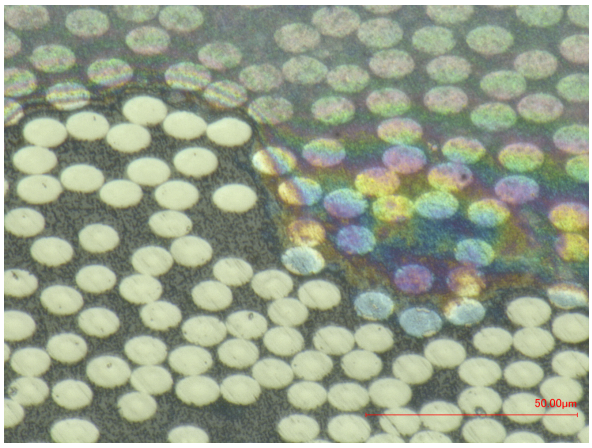

(b) Dipcoating with 100nm polystyrene spheres (Keyence VHX-2000 at magnification 2000x)

Figure 3.4: Results of dipcoating on carbon fiber composite

The evaluation for this method is the same as for the drop deposition: bad distribution due to the coffee ring effect, average repeatability due to manual dipping, and very high ease of use without special equipment. Furthermore, the Aerosil nanoparticles are too small to be seen by the optical microscope, while forming a network that covers the whole area. This does not happen for the polystyrene spheres, as they are still distinguishable in the images.

3.3.3. Electrospraying

Looking for a better distribution of the nanoparticles, electrospraying has been checked. The setup is shown in Figure 3.5. A syringe is filled with nanoparticles dispersed in demineralized water. This syringe is put in a device which steadily pushes out the liquid through the needle at a constant rate. This needle is electrically charged by a cable, putting a controlled high electrical potential between the needle and the earthed metal plate. Then charged drops are emitted from the tip of the needle which are attracted to the earthed metal plate. Therefore different specimens are placed on this plate. Because of the high voltage, the droplets coming from the needle reach a high velocity before striking the surface. It is a very controllable process which involve these process parameters:

Distance needle - target The distance between the needle and the earthed plate with the specimens. *10-20 cm*

Voltage The electric potential applied to the needle, in Volts. *7.5-20 kV*

Liquid The liquid used, especially the concentration of nanoparticles in it. *Demineralized water*

Feeding rate The rate with which the liquid is pushed out of the syringe. *0.1-0.5 ml/h*

Time How long the spraying is done, important for the speckle density. *0-10 min*

Figure 3.5: The electrospraying setup.

Since there are a lot of parameters involved in this process, a first trail with the nanoparticles is done on glass slides (which are normally used in microscopy). The result can be seen in Figure 3.6. In the drops, the particles are nicely distributed, but at the edge, the coffee ring effect is still visible.

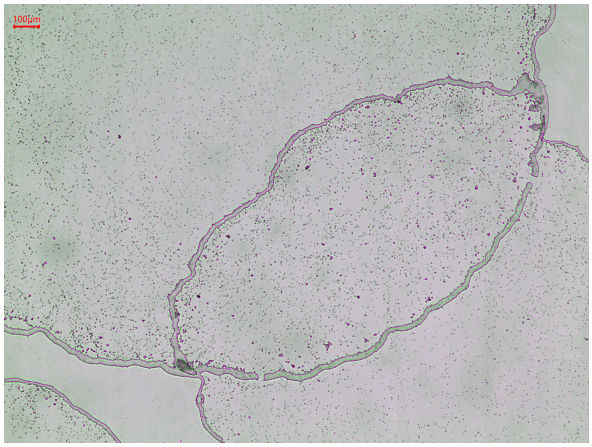

Figure 3.6: Overlapping drops on a glass slide.

With the improved process parameters (distance 13 cm, voltage 20 kV, dispersion with 0.5 drop/ml (fine pipette) 500 nm polystyrene spheres, feeding rate of 0.5 ml/h and time 10 minutes), carbon and glass fiber specimens were also sprayed. Results of this are displayed in Figure 3.7. As can be seen in Figure 3.7a, drops are still formed. Looking closer in Figure 3.7b shows that there is a coffee ring at the edge, but inside the drop, the distribution of particles is good. For the glass fiber, the results are very bad, since only 1 drop could be found on the surface. This is because it is not conductive, as where the carbon fibers are. Because of this non-conductivity, the glass fiber specimen is not attracting droplets.

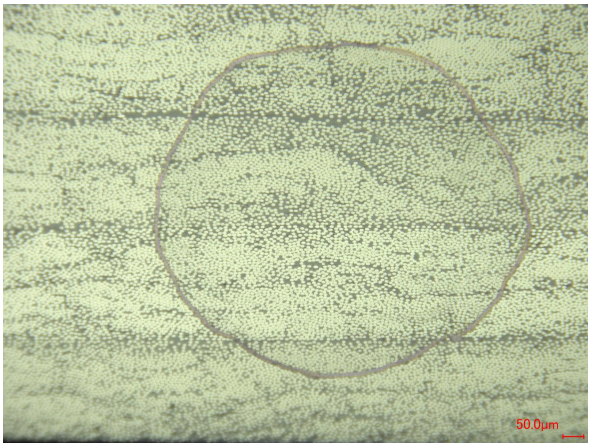

(a) An electrosprayed drop on a carbon fiber specimen (Keyence VHX-2000 at magnification 250x)

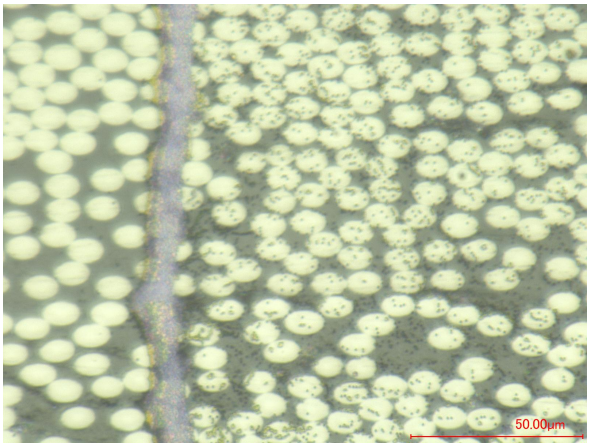

(b) Close up of the drop edge (Keyence VHX-2000 at magnification 2000x)

Figure 3.7: Results of electrospraying on a carbon fiber specimen

If this method is held against the quality criteria, it can be concluded that the distribution of the speckles is not good, since drops are still formed, with the coffee ring effect at play. Furthermore it scores good on repeatability, since the process does not require any manual actions during spraying. Finally, the ease of use is very low, since specialized equipment is needed, and a lot of parameters have to be tuned. Another point for which the ease of use is low is the time, since after 10 minutes the specimens are still far from fully covered.

3.3.4. Airbrushing

Airbrushing is a method that has been used a lot to produce speckle patterns for DIC on larger scales, with paint [18]. For micro-scale DIC, these paint speckles are of course too large (3 to 50 µm), but the airbrush can also be used to spray nanoparticles as a speckle pattern [39]. The airbrush uses compressed air to nebulize a liquid (the dispersion with nanoparticles) in a spray towards the specimen.

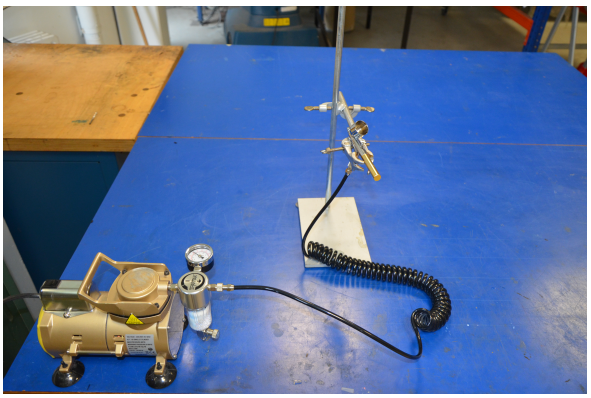

(a) The overall components of the airbrushing system: compressor, connector hose and spray-gun.

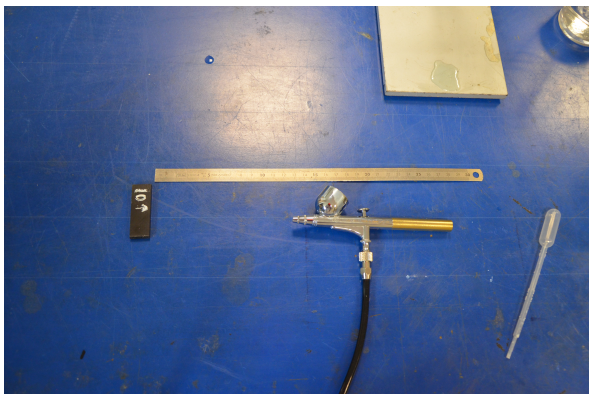

(b) Close-up of the spray gun and a specimen.

Figure 3.8: The airbrushing setup.

Airbrushing is a manual process. It involves multiple parameters, of which many are controlled manually. These parameters are:

Specimen position Distance, where in spray cone the specimen is held. *Manual control*

Speed The speed with which the spray gun is moved relative to the specimen surface. *Manual control*

Feeding rate The rate flow of the dispersion fed into the spray gun, determined by how far the trigger is pulled back. *Manual control*

Pressure Pressure set on the compressor.

Dispersion The mixture used in the airbrush.

Amount of layers The amount of times a layer is sprayed on the specimen, determining the speckle density.

The first trials indicated that when spraying, drops are formed which then impacted the specimen, as seen in Figure 3.9a. To improve the wetting of the drops, as explained in 2.3, isopropanol is added to the dispersion of nanoparticles. With the right process parameters, drop forming on the surface stops, and complete wetting of the specimen surface occurs. When this happens, a nanoparticle distribution as in Figure 3.9b occurs. On a smaller scale, the distribution can be seen in Figure 3.9c.

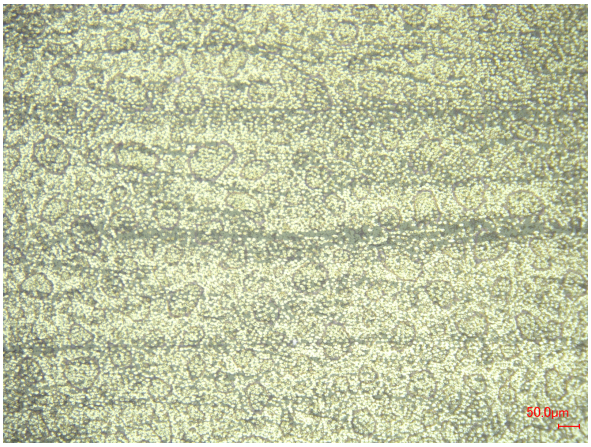

(a) Result of airbrushing with 500 nm polystyrene spheres dispersed in demineralized water, Keyence VHX-2000 at magnification 250x.

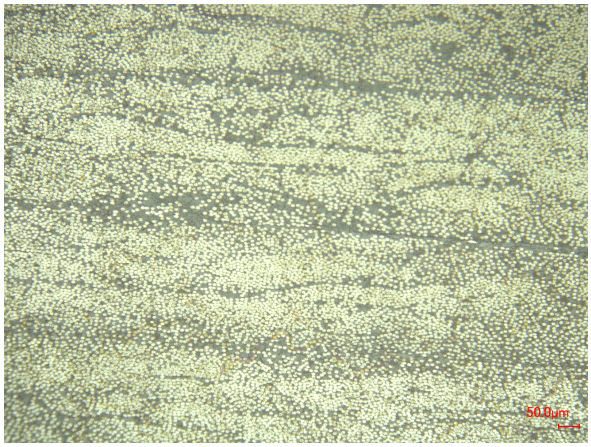

(b) Result of airbrushing with 500 nm polystyrene spheres dispersed in a mixture of isopropanol and demineralized water, Keyence VHX-2000 at magnification 250x.

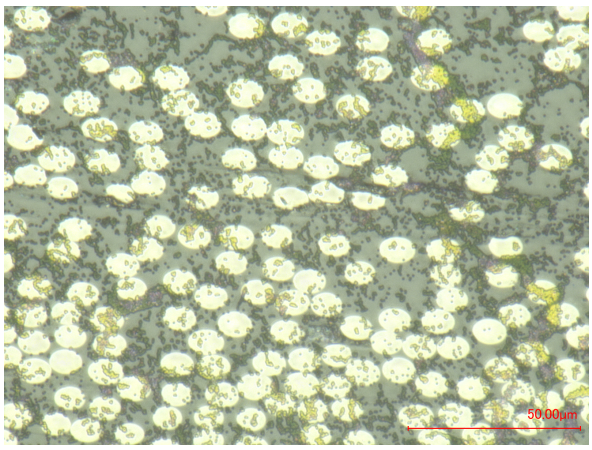

(c) Result of airbrushing with 500 nm polystyrene spheres dispersed in a mixture of isopropanol and demineralized water, Keyence VHX-2000 at magnification 2000x.

Figure 3.9: Difference between dispersing nanoparticles in water or in a mixture of water and isopropanol.

First trials of this method indicated that, when adding isopropanol to the dispersion, drop forming on the specimen surface can be eliminated. This leads to a good distribution of speckles. The drawback of this method is that multiple parameters are determined by the operator, since it is a manual process. Therefore, the repeatability is not good and experience is needed. Finally, the ease of use is good, since only the airbrush is needed, which is easy in use and available in the lab. To achieve a good speckle density, the amount of layers can be tuned, which is elaborated on in Section 3.5.

3.4. Method selection

In previous sections, different speckle applications are evaluated. Combining conclusions from previous subsections, a summary of the scores for each method is given in Table 3.1 by using plusses and minuses. As the most important criteria is the distribution of the speckles, and after that the ease of use, the airbrushing is the most suitable speckle application method, which is optimized in Section 3.5. Comparing the Aerosil and polystyrene microspheres, the polystyrene spheres are preferred, since these particles can be seen distinctly in an optical microscope, contrary to the Aerosil.

Table 3.1: Comparison of the different speckle application methods.

		Distribution	Repeatability	Ease of use
Template Patterning		+/-	+/-	–
Nanoparticle Patterning	Drop deposition	-	+/-	++
	Dip-coating	-	+/-	++
	Electrospraying	+/-	+	-
	Airbrushing	+	-	+

3.5. Optimization of airbrushing nanoparticle deposition

Now that airbrushing polystyrene microspheres is chosen as the preferred method to create a speckle pattern, the method has to be optimized. As mentioned before, the absence of drops on the surface during the process is crucial to ensure a good distribution of the speckles. This is influenced by all parameters, except for the amount of layers. Regarding the specimen position, if it is too close to the spray gun, too much liquid is nebulized on it, forming drops. If it is too far away, not enough particles from the spray cone hit the specimen. A distance comparable to the one used for paint airbrushing is suitable, which is around 10 cm. The speed with which the spray gun is moved is similar to paint airbrushing as well, but has be high enough so that areas do not get too wet, because drops will forms. As a lot of parameters are controlled manually, experience is needed for this. As nebulizing too much liquid leads to drops forming, the feeding rate has to be kept minimal. The pressure on the airbrush determines the velocity of the nebula flowing out, which has to be high. 2 bar is used, as this is the maximum which the compressor can steadily supply. Regarding the dispersion, adding isopropanol improves the wetting, but there is also a drawback. Using too much isopropanol leads to deterioration of the polystyrene spheres. When diluting the dispersion of the manufacturer with only isopropanol and putting a drop on the surface right after, the microspheres already are deteriorated, as seen in Figure 3.10. To solve this, it is first dispersed with more demineralized water, and right before airbrushing, with isopropanol. A mixture that works well is using 8 fine drops of the nanoparticle dispersion per ml of water, and mixing 2 drops (normal pipette) of it with 9 drops of isopropanol (normal pipette) in the spray gun of the airbrush. As the normal pipette drops 30 drops per ml of water and 60 drops per ml of isopropanol, the volume ratio of the mixture is 4:9.

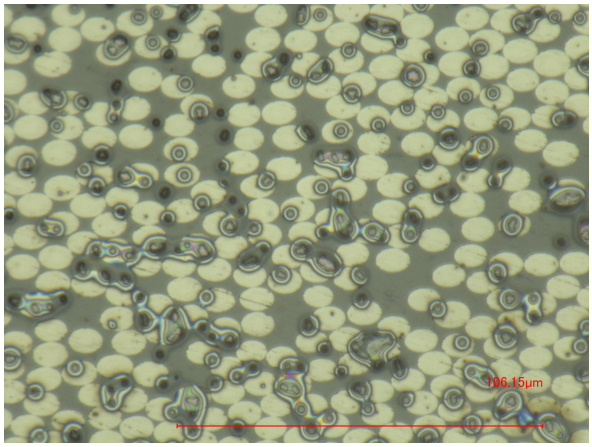

Figure 3.10: Polystyrene microspheres of 1 µm, dispersed in pure isopropanol and drop deposited on a carbon fiber composite right after mixing.

Another problem that occurred is the clustering of particles, as seen in Figure 3.11a. Especially with bigger spheres this is detrimental for the speckle pattern, since the pattern is not distributed uniformly anymore, and also not random. A solution to this problem is ultrasonification. The high frequency vibrations break up the bonds between the spheres. Although clustering is still present, it is less than without ultrasonification, as displayed in Figure 3.11b.

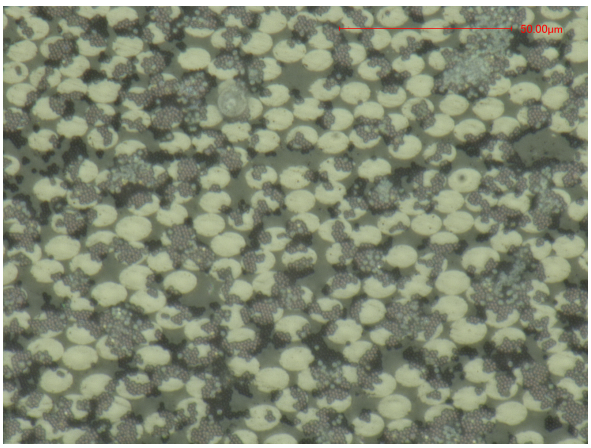

(a) Result of airbrushing 1 µm polystyrene spheres on a carbon fiber specimen, without ultrasonification (Keyence VHX-2000 at magnification 2000x).

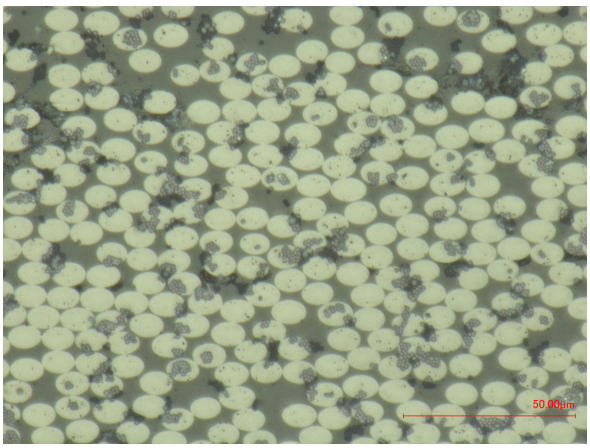

(b) Result of airbrushing 1 µm polystyrene spheres on a carbon fiber specimen, with 5 minutes ultrasonification (Keyence VHX-2000 at magnification 2000x).

Figure 3.11: Influence of ultrasonification on nanoparticle clustering.

With the distribution issues (drop forming and clustering) solved, the optimal speckle density has to be found. One parameter in the airbrushing process is still not determined, which is the amount of layers airbrushed on the specimen, since 1 layer is clearly not enough, as seen in Figure **??**. To optimize this, a method to quantify how good a speckle is first has to be defined. To do this, images of the speckle pattern are taken and a virtual displacement is applied to it. This is done by shifting every pixel 23 pixels (the size of a subset) to the right. After that, the Vic2D correlation algorithm is applied to the images (the original and virtually displaced one). For every subset, Vic2D outputs a match confidence, which is the 1-standard deviation confidence for the match in pixels. Over the image, the average of this value is taken as a measure for the quality of the correlation, depending on the speckle. Since it indicates the standard deviation, the match confidence value should be kept as low as possible. For the correlation, a subset size of 23 pixels is taken, as this is roughly the size of half a carbon fiber. Results are summarized in Table 3.2. For this subset size, the polystyrene spheres of 500 nm and 100 nm deliver the best results, whereas those of 1 µm are not improving the correlation in comparison to a clean specimen (where only the polishing is applied). The Aerosil delivers results in between.

Table 3.2: Match confidence results as function of nanoparticle type and amount of layers.

Nanoparticle					
Polystyrene, 1 µm	Layers	20	**24**		
	Match confidence	0.0869	**0.0860**		
Polystyrene, 500 nm	Layers	6	**9**	12	
	Match confidence	0.0663	**0.0588**	0.0598	
Polystyrene, 100 nm	Layers	2	3	**4**	5
	Match confidence	0.0610	0.0603	**0.0550**	0.0659
Aerosil R972	Layers	4	**8**	16	32
	Match confidence	0.0688	**0.0620**	0.0675	0.0687
None (clean specimen)	Match confidence	0.0864			

Finally, the optimal results are achieved when polystyrene spheres are used. If the ones of 100 nm are used, 4 layers should be applied, and for the 500 nm spheres, 9 layers should be applied. Nevertheless, since a lot of parameters are influenced by manual actions, a microscope should be held close to check the speckle density in between different amount of layers. Optimized speckle patterns are shown in Figure 3.13. Furthermore, to better understand how the nanoparticles are arranged on the specimen surface, SEM images are provided in Figure 3.14. Images are made with the the JEOL 7600F SEM, on which is elaborated in Chapter 4. For each type of composite used (Carbon Fiber (CF) and Glass Fiber (GF) and each size of polystyrene sphere (0.1, 0.5 and 1 µm), images are made with the secondary electron detector. An accelerating voltage of 2kV is used, and the magnification of 5000x is kept constant through the images. On the images, it is clearly visible that the particles form clusters. Furthermore, sometimes a microsphere is stacked on top of the others. Both phenomena seem to happen more often with smaller particles. Furthermore, in Figure 3.14b, the clustering of 100 nm happens severely on the GF, which is not the case on CF as seen in Figure 3.14a.

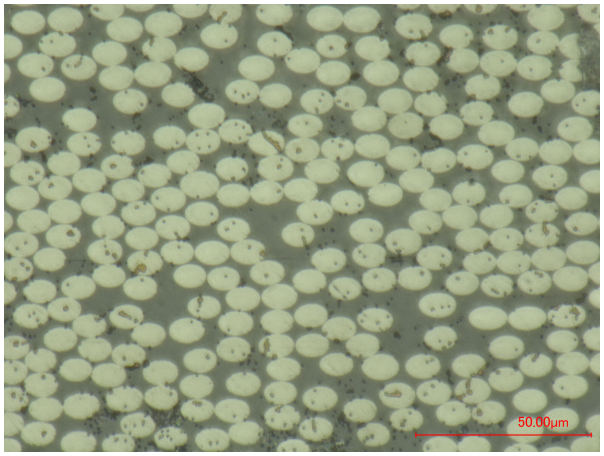

Figure 3.12: The speckle pattern after 1 layer of 100 nm polystyrene spheres on a carbon fiber specimen (Keyence VHX-2000 at magnification 2000x).

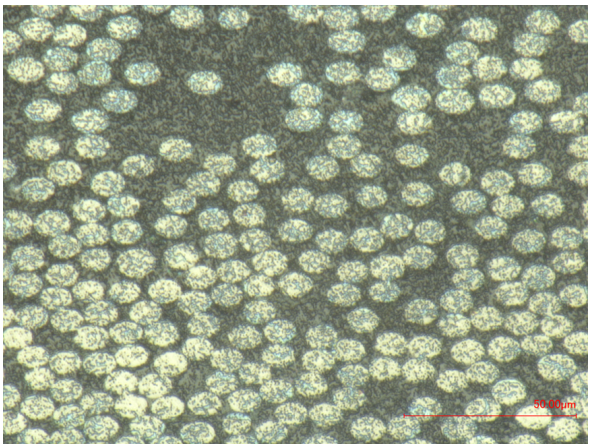

(a) Result of airbrushing 4 layers of 100 nm polystyrene spheres on a carbon fiber specimen (Keyence VHX-2000 at magnification 2000x).

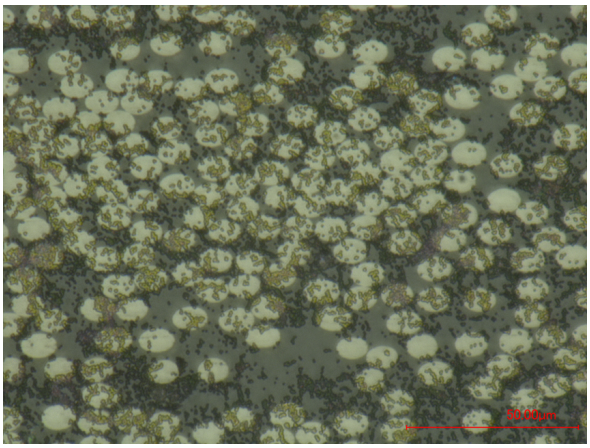

(b) Result of airbrushing 9 layers of 500 nm polystyrene spheres on a carbon fiber specimen (Keyence VHX-2000 at magnification 2000x).

Figure 3.13: The optimized speckle patterns.

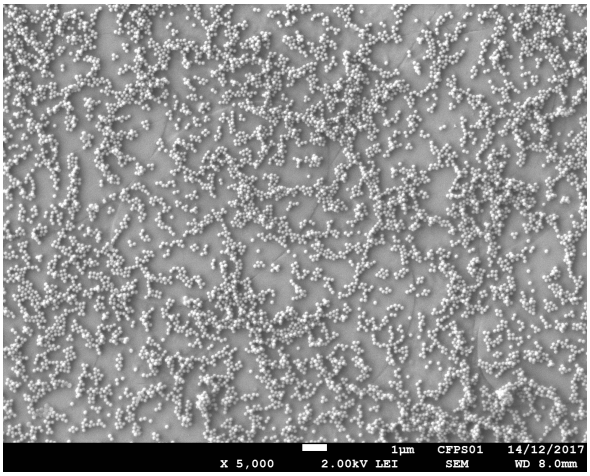

(a) Carbon fiber, 100 nm polystyrene spheres.

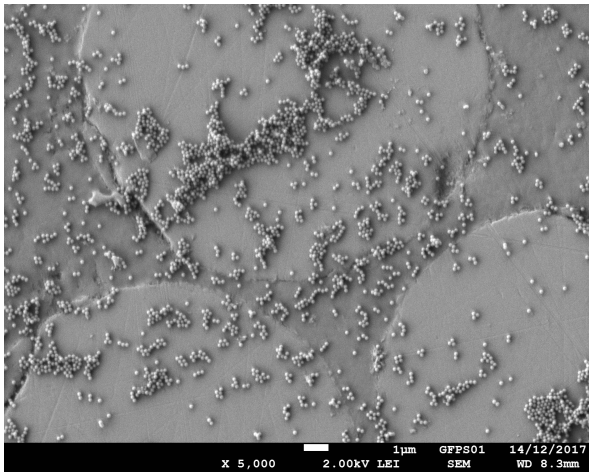

(b) Glass fiber, 100 nm polystyrene spheres.

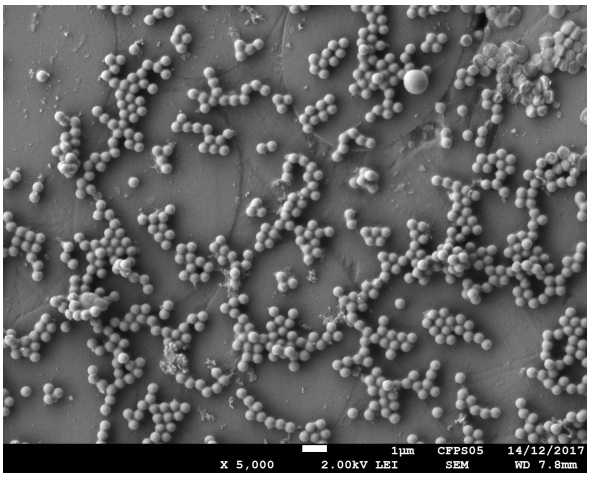

(c) Carbon fiber, 500 nm polystyrene spheres.

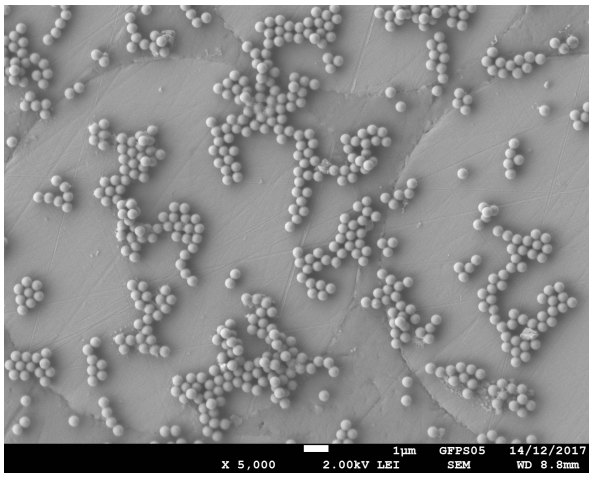

(d) Glass fiber, 500 nm polystyrene spheres.

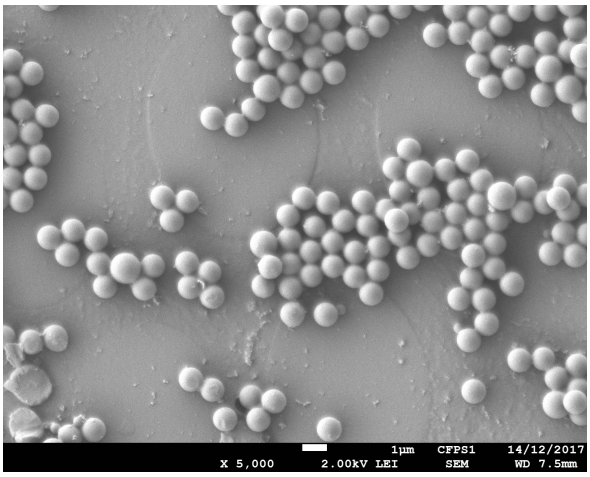

(e) Carbon fiber, 1 µm polystyrene spheres.

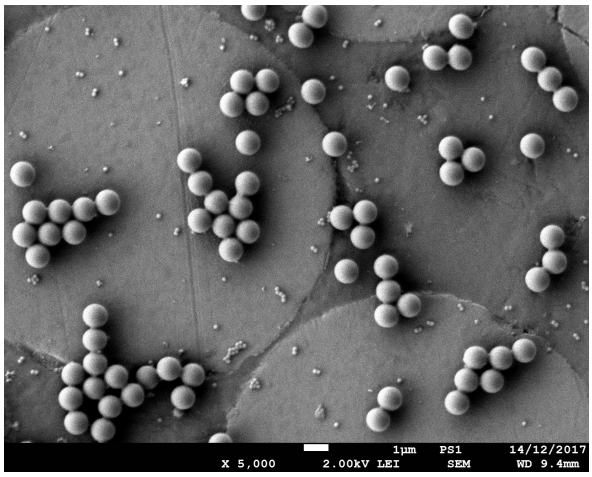

(f) Glass fiber, 1 µm polystyrene spheres.

Figure 3.14: SEM images of the speckle pattern after airbrushing with polystyrene microspheres (magnification 5000x).

3.6. Statistical speckle analysis

In this section, a more detailed analysis of the speckle patterns produced by different techniques from Section 3.2 and 3.3 is performed. The same is done for the optimized airbrushed patterns from Section 3.5.

3.6.1. Methodology

To come to usable statistics of an image, which are the speckle sizes, the image has to be processed first. For this, the image processing software package ImageJ [25] is used. First, images are binarized in black and white, by using the local threshold method from ImageJ. This algorithm calculates the median grey value of the pixels around the pixel of interest in a circle with radius 15. This radius is chosen because it corresponds roughly to the size of a subset in the remainder of the project. If the pixel value is at least 10 higher than the median, it is colored black, otherwise white. This way the contrast can be looked at in a local manner, which is needed because the color of the particles on matrix of fibers is different, and the background color is as well. Examples of this binarization are shown in the remainder of this section.

The next step is to count the particles, which is done by the same software. In the binarized images, the algorithm checks which black pixels are connected to determine the size of the particles. This produces a list with the sizes of the speckles, on which a statistical analysis is performed by a histogram, to look at the distribution of the sizes.

3.6.2. Statistics & comparison of speckling techniques

In general, the sputtering provides low contrast images, which is reflected in Figure 3.15a. Only few pixels have enough contrast to be colored black by the algorithm. These are mostly single pixels. Therefor, the histogram has a large spike in the first bin. Furthermore, the calculated coverage is only 0.3 %. The sputtering technique thus does not provide a good result.

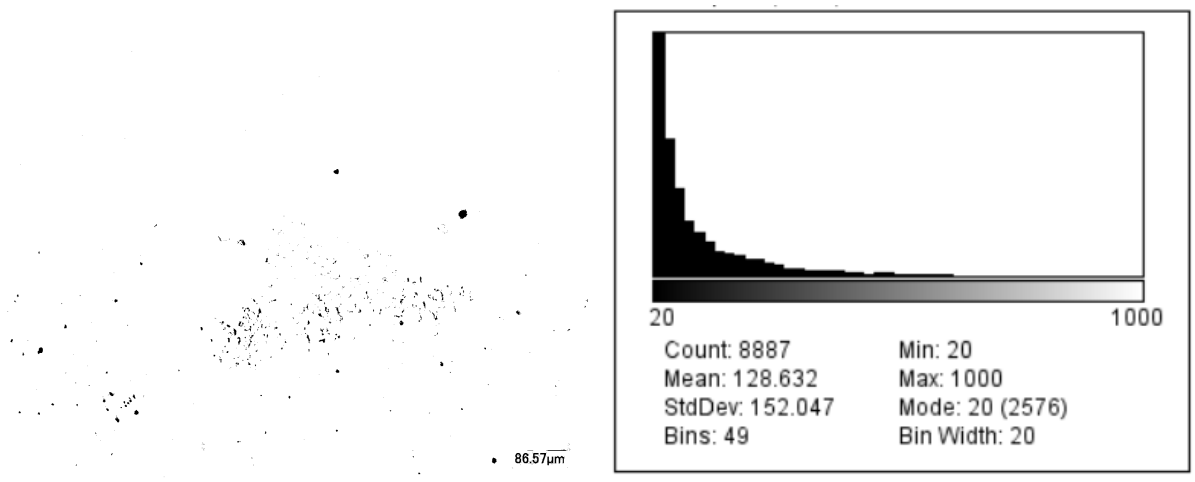

(a) Image from Figure 3.2b binarized with ImageJ. 0.3 % coverage.

(b) Histogram of the binarized image.

Figure 3.15: Statistical analysis for the sputtering.

As seen in the original image in Figure 3.16a, created with drop deposition, a thick layer of multiple layers of spheres is formed in the lower half of the image. Furthermore, to the right, this causes a reflection. In the binarized image in Figure 3.16b, this is reflected in very small black spots in this area. Coverage is 12.9 %, which is relatively good. The histogram has a large first spike as well because of the large amount of single pixels or very small (smaller than the used particles) areas with contrast. The quality of this speckle pattern is thus not good.

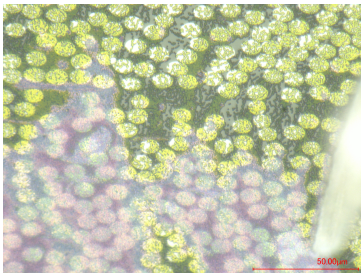

(a) Original image.

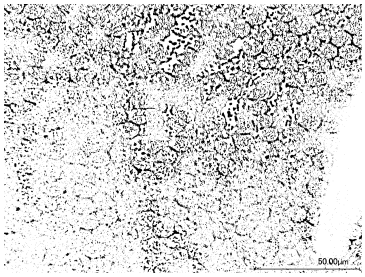

(b) Image from drop deposition binarized with ImageJ. 12.9 % coverage.

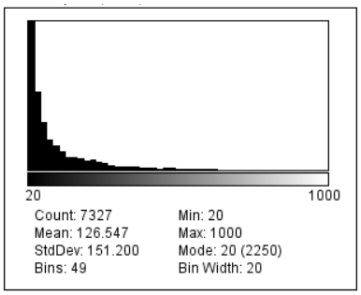

(c) Histogram of the binarized image.

Figure 3.16: Statistical analysis for drop deposition.

When dipcoating with Aerosil is used, almost no speckles are visible in the binarized image in Figure 3.17a. This is because of the low contrast, and is also seen in the low coverage of 6.4%. Most contrast is provided by the fiber edges. Lots of small particles, due to algorithm. The histogram in Figure 3.17b also has a clear large first peak, but no different other information. This method also does not provide a good speckle pattern.

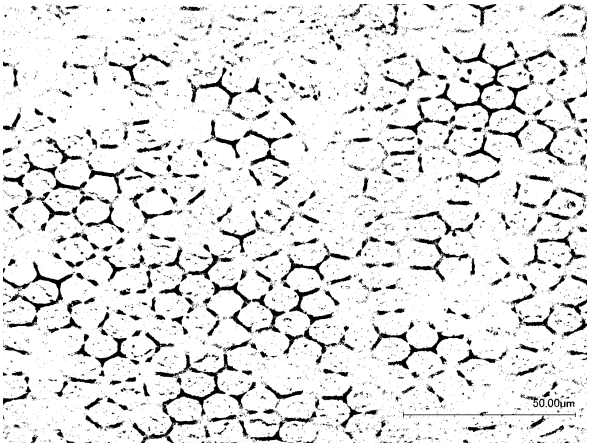

(a) Image from Figure 3.4a binarized with ImageJ. 6.4 % coverage.

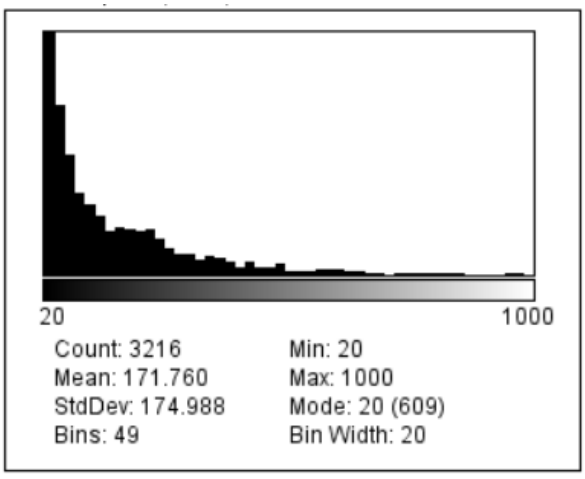

(b) Histogram of the binarized image.

Figure 3.17: Statistical analysis for dipcoating with Aerosil.

For the dipcoating with polystyrene microspheres, the speckles on the matrix provide good contrast as seen in Figure 3.18a. There are only very few speckles on fibers. On the upper right, a thick particle layer provides poor contrast, together with a reflection as seen in Figure 3.4b. Because of the high amount of microspheres in the image, the coverage is still relatively high (9.4 %). As before, the histogram in Figure 3.18b shows only a large first peak. The quality is not good here.

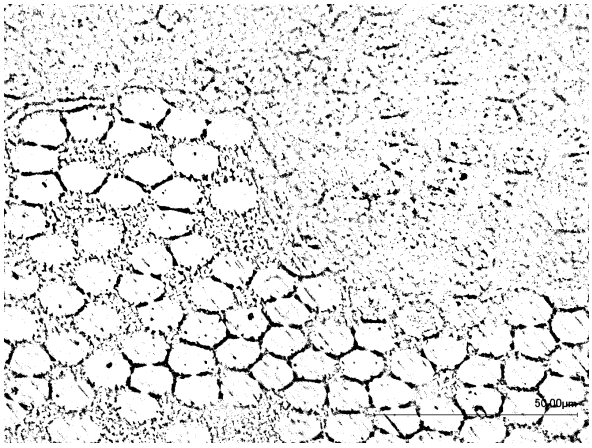

(a) Image from Figure 3.4b binarized with ImageJ. 9.4 % coverage.

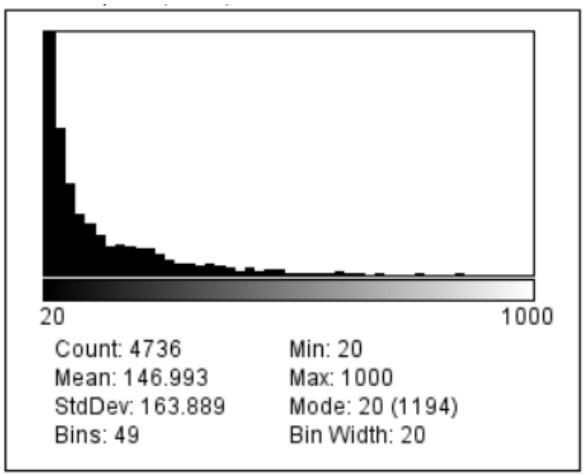

(b) Histogram of the binarized image.

Figure 3.18: Statistical analysis for dipcoating with microspheres.

For the electrospraying, different areas can be distinguished, as well in the binarized image in Figure 3.19a as in the original in Figure 3.7b. There is a unspeckled portion to the left, where only fiber edges provide contrast. To the right, there is a good distribution inside the drop with particles. The drop edge consists of a thick layer of microspheres. As expected, the edge has a bad contrast as well. Overal, the coverage of 12.7% is good. From the histogram of Figure 3.19b, the usual first spike is clearly present, but after this spike, there are some bins with a relative high amount in it. This is because the area inside the droplet is speckled very well, and the microspheres are well distributed there.

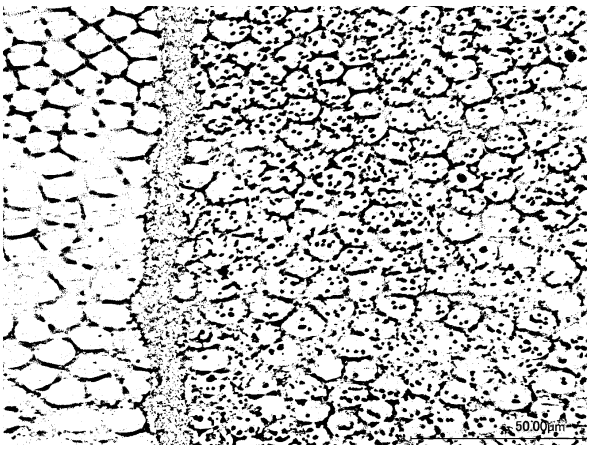

(a) Image from Figure 3.7b binarized with ImageJ. 12.7 % coverage.

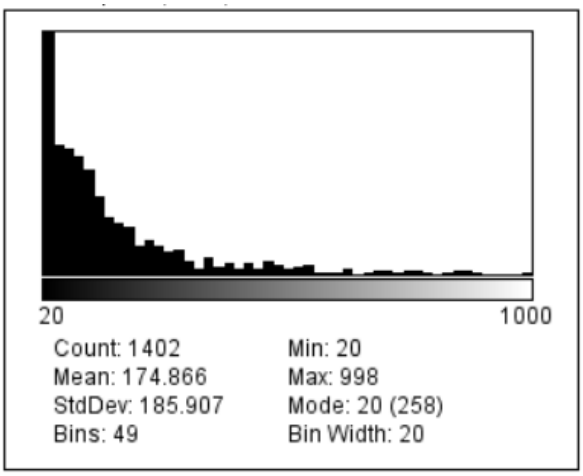

(b) Histogram of the binarized image.

Figure 3.19: Statistical analysis for electrospraying.

For the airbrushing, the fiber edges are hardly noticable in the binarized image in Figure 3.20a. The distribution seems even over the area, and the coverage is highest of all methods, with 16.3% coverage. In the histogram in Figure 3.20b, not only the first spike is high (which can be due to the algorithm), but the second, third and further as well. The most real speckles are in this image. This method provides thus best speckle pattern, which corresponds to the conclusion of Section 3.4.

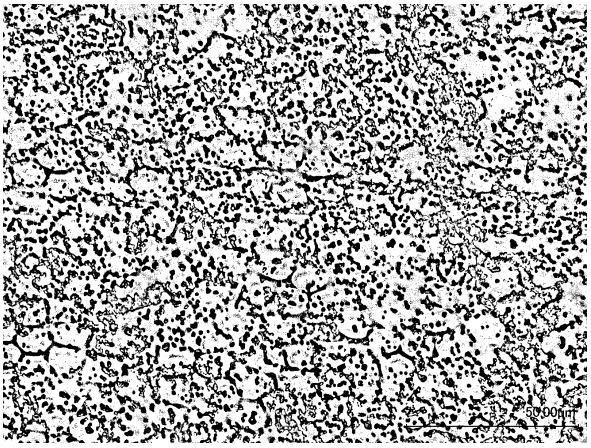

(a) Image from Figure 3.9c binarized with ImageJ. 16.3 % coverage.

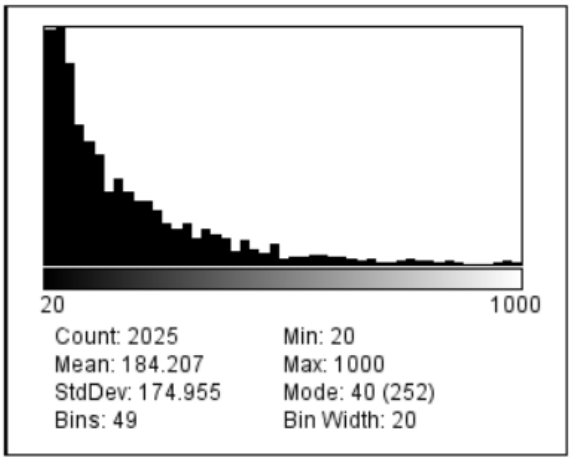

(b) Histogram of the binarized image.

Figure 3.20: Statistical analysis for electrospraying.

3.6.3. Statistics & comparison of optimized airbrushing

The same methodology as described before is also used to produce the speckle size histograms in Figure 3.21. One slight modification is made, which is the bin width of the histogram. Because different microsphere sizes are used, the bin width is set to the size of 1 microsphere. In this way, the degree of clustering of the microspheres can be compared, even with different sphere sizes. If the histograms in Figure 3.21 are compared, Figure 3.21a and 3.21b are similar, and very skewed to the left. This corresponds with a lower degree of clustering (more single spheres, and a some clusters with only a few spheres). If they are compared to Figure 3.21c, the tail on the right side of the histogram is significantly larger. This means a lot of very large speckles are present, which is due to the clustering of the microspheres.

Furthermore, it is checked whether these statistics correlate to the *Match Confidence* used in Section 3.5. In Table 3.2, the corresponding Match Confidence for the 3 sizes are shown. The results for the optimal amounts of layers are 0.0550, 0.0588 and 0.0860 for respectively the 100 nm, 500 nm and 1 µm spheres. The 1 µm spheres clearly perform worst here, which is also seen in the histogram, as more clustering is present. Between the 100 nm and 500 nm, the difference is small in comparison to the difference with the 1 µm, but nevertheless present. The 100 nm perform slightly better in Match Confidence, which is also noted in the histogram, where slightly more clustering is present with the 500 nm spheres. From this can be concluded that the Match Confidence method and the statistical analysis performed in this section deliver similar results.

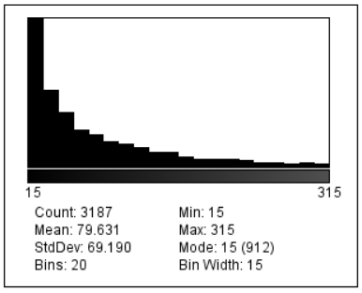

(a) Histogram of speckle sizes after airbrushing 4 layers of 0.1µm polystyrene microspheres. Based on image from Figure 3.13a.

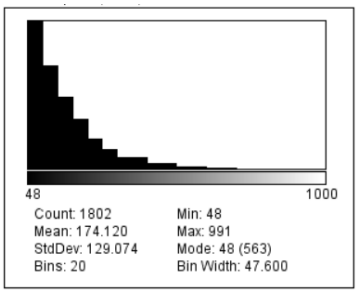

(b) Histogram of speckle sizes after airbrushing 9 layers of 0.5µm polystyrene microspheres. Based on image from Figure 3.13b.

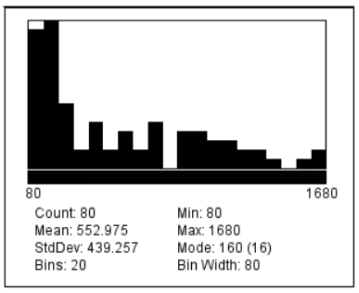

(c) Histogram of speckle sizes after airbrushing 24 layers of 1µm polystyrene microspheres.

Figure 3.21: Histograms of created speckle sizes of the optimized airbrushing procedure.

3.7. Conclusion

To find the best speckle application method, 2 methods are used. The first one evaluates the method based on 3 qualitative criteria. Based on this, template patterning and nanoparticle patterning methods are held against each other. The nanoparticle patterning with the airbrush is the most suitable one. To further optimize the parameters involved with this method, a quantification for speckle quality is performed with the built-in match confidence parameter in Vic2D. Using this, the optimal amount of layers is determined for each size of nanoparticle. The nanoparticles used are polystyrene microspheres, of size 100 nm, 500 nm and 1 µm. Using a statistical method, the different techniques are analysed as well. This confirmed that the airbrushing is the best technique, in combination with 100 nm or 500 nm polystyrene microspheres.

4

Digital microscopic imaging system

4.1. Comparison between optical and SEM imaging

To make images for DIC, two inherently different imaging systems are available, an optical and a SEM system. The optical imaging system available is the Keyence VHX-2000 digital microscope, equipped with the Z250 lens system, elaborated on in Section 4.1.1. The SEM system is the JEOL 7600F, explained in Section 4.1.2. The most important parameters of the systems are listed in Table 4.1. Images from both systems have been tested with DIC in the following sections. Based on these results and the parameters of Table 4.1, an imaging system is chosen.

4.1.1. Keyence VHX-2000 digital microscope

The Keyence VHX-2000 is a digital microscope. Instead of using an ocular where the microscope operator can look through, a 54 megapixel 3CCD camera is used to capture images, which are displayed on the monitor. During the thesis project, the VH-Z250R/W lens system is used. With this lens, magnifications from 250x to 2500x are possible. The system further consists of various input instruments (mouse, keyboard and controller), and the stage, on which specimens are placed. This stage can move in its own plane (x- and y-direction) since it is equipped with stepper motors, controlled by the joystick of the controller. The lens is attached to a stepper motor as well to provide movement of the lens in z-direction, which is needed to focus the image. This is controlled by the turning knob on the controller, or by an algorithm if the 'autofocus' feature is used. All parts are indicated in Figure 4.1.

Table 4.1: Specifications of the different imaging systems

	Keyence	JEOL SEM
Best resolution	250 nm	1.5 nm
Pixel size	min. 86 nm	min. 1.5 nm
Magnification	250-2500x	25-1000000x
FOV (pixels)	1600x1200	max. 5120x3840
FOV (size)	min. 140x100 µm	Depending on magnification

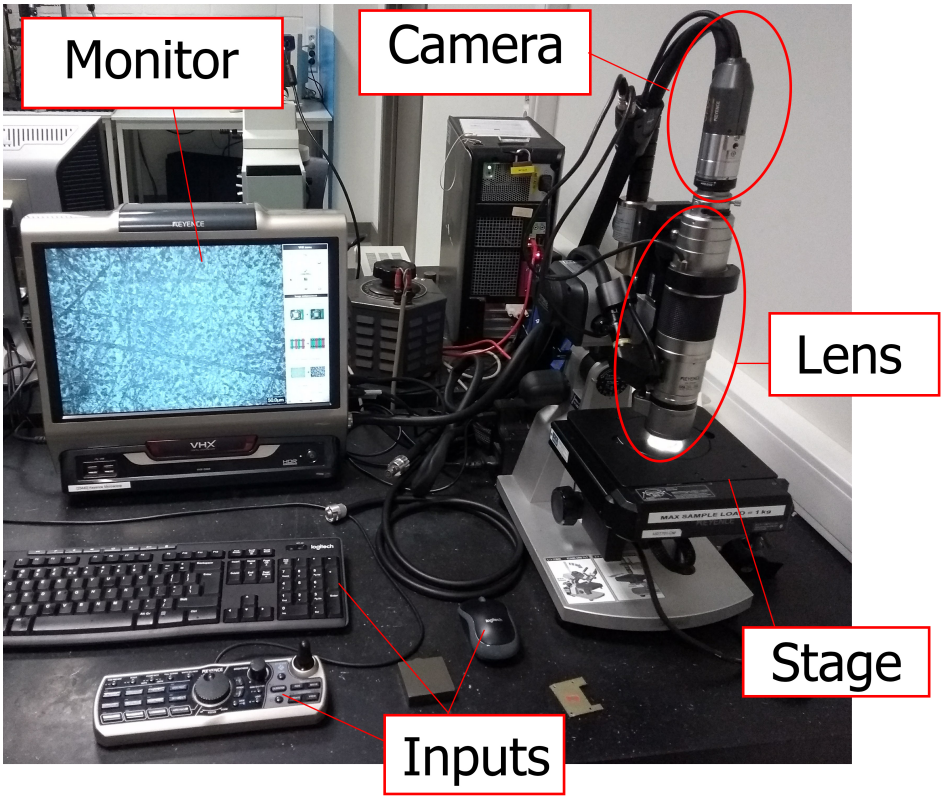

Figure 4.1: The setup of the Keyence VHX-2000 digital microscope, equipped with the Z250 lens system.

Through the project, images are made in the same experimental conditions, although different magnifications are used. For images on which DIC is applied (magnification 2000x), brightfield illumination is used, with a shutter time of 1/250s. Color temperature is set at 2700K, and focusing performed without autofocus.

4.1.2. JEOL 7600F SEM

Instead of light rays, SEM uses an electron beam to create microscopic images of a specimen. Using electromagnetic lenses, the electron beam is steered over the surface, and reflected electrons are captured to form the image. For more information regarding the working principle of a SEM, and how this affects DIC, the reader is referred to [14], [34] and [35]. A conclusion that is drawn from these sources is that the scanning nature of how SEM images are made leads to a more intricate distortion pattern than in optical microscopy.

For SEM imaging, a JEOL 7600F microscope is available, which is depicted in Figure 4.2. On the right side, the computer, screen and input console to control the SEM microscope can be seen. On the left side, the vacuum chamber and electromagnetic components are seen, which are supported by a vibration isolating table. Before imaging, specimens are coated with a conductive gold layer to reduce the charging of the specimen. This is done for 30 seconds in a magneto sputtering device, after polishing, cleaning and speckling of the specimen. Nevertheless, the accelerating voltage is kept as low as possible to further reduce charging effects. Exact imaging settings are always saved in the SEM images, in the black bar at the bottom of each image.

Figure 4.2: The JEOL JSM 7600F SEM microscope [12].

4.1.3. Preliminary test results, optical system

A baseline test is taken 100 stationary images of a CF specimen (100 nm polystyrene spheres) with the Keyence in the lab (magnification 2000x) and running the DIC algorithm of Vic2D on it. Subset size is 29 pixels, step size 11 (amount of pixels between subsets) and strain filter 15 (amount of subsets over which the strain is calculated), as these these settings have proven to give good results for normal scale DIC by experience. With this, an average (over the 100 images) displacement standard deviation x-direction of 12.4 nm is achieved. Only the strain in 1 direction is shown, because the same is done for the SEM and an average strain in x-direction standard deviation of 924 $\mu\epsilon$ (931 $\mu\epsilon$ in y-direction). The average of the minima of the strain is 9370 $\mu\epsilon$, and the average of maxima 10186 $\mu\epsilon$. A typical displacement field is displayed in Figure 4.3a, and a corresponding strain field in Figure 4.3b.

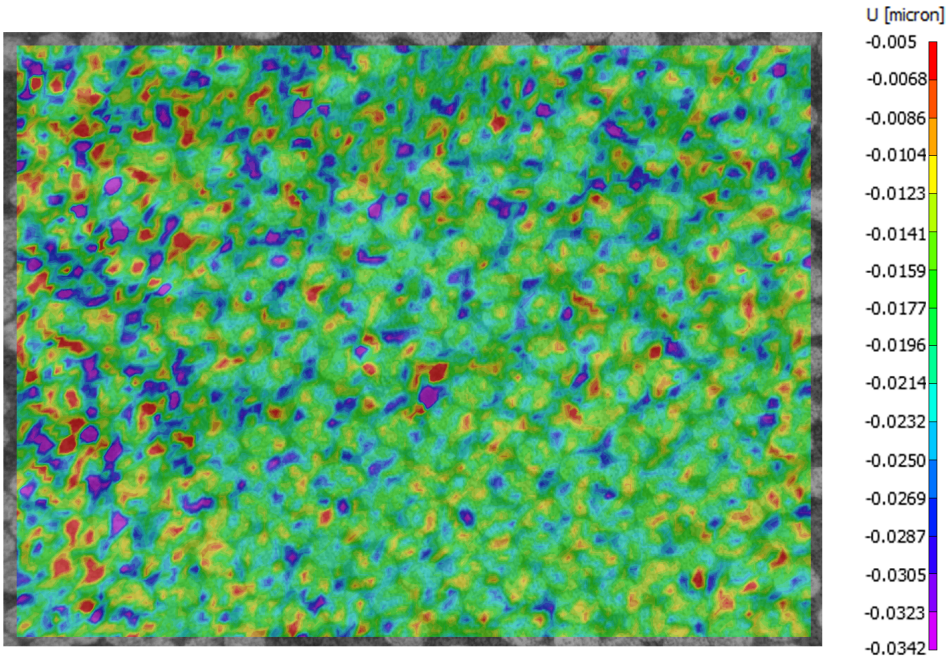

(a) The horizontal displacement field.

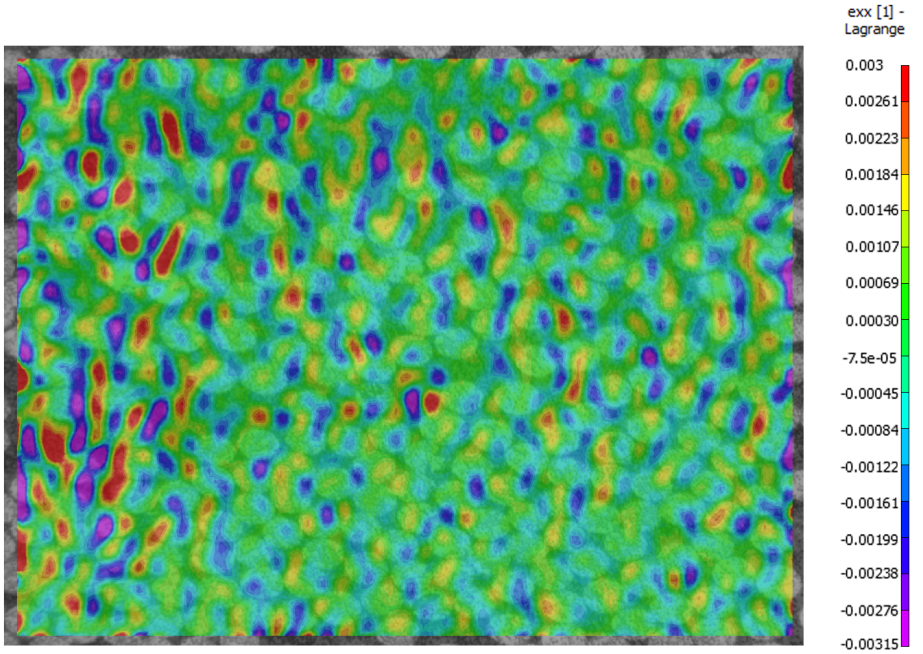

(b) The horizontal strain field.

Figure 4.3: Preliminary DIC results of the optical system.

As seen in Figure 4.3, regions with higher false displacements also have more false strains present. Furthermore, in Section 1.5 it is assumed that the distribution of the displacements is a normal one. This is checked now by plotting the displacements of the subsets of the first image in Figure 4.4. As seen in this figure, the distribution is close to normal. However, it is still not accurate enough. Another remark is made about the mean displacement: although no displacement is applied to the specimen, the mean displacement is not zero. The cause for this is probably a vibration induced displacement between the reference image and the correlated image.

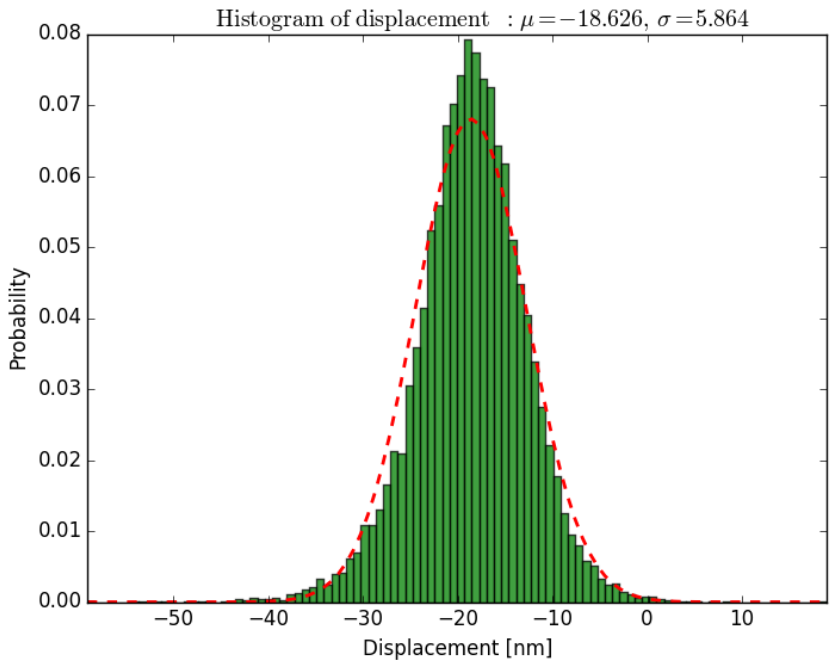

Figure 4.4: The displacement distribution of the first image in the series.

4.1.4. Preliminary test results, Scanning Electron Microscope

A baseline test with the SEM is also performed. Using a CF specimen, speckled with 100 nm polystyrene microspheres, images of magnification 500x are taken with the JEOL 7600F SEM. DIC was performed with Vic2D, using subsets of 55 pixels, step size 19 and strain filter of 15. This gives the subsets the same physical size as for the optical system, since the SEM has finer pixel resolution at this magnification. Imaging parameters are displayed together with the results in Figure 4.5.

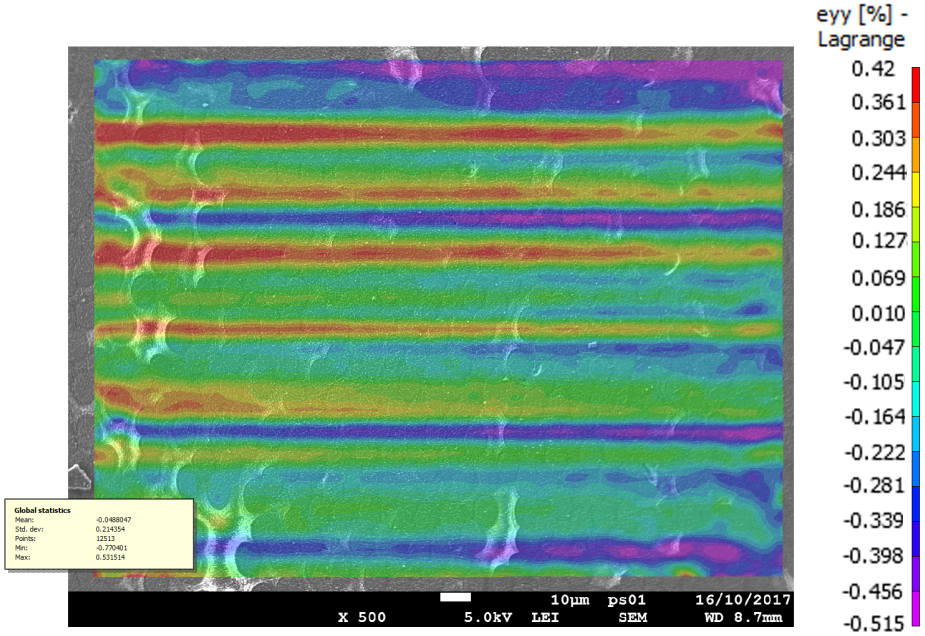

Figure 4.5: Strain in y-direction when DIC is applied on the SEM images.

In Figure 4.5, a pattern is clearly visible, coming from the imaging mechanism used by the SEM, as described in the Literature Study [28]. This happens especially in y-direction, since the repositioning of the electron beam to a new line takes a significant amount of time, during which drifting occurs [33]. The standard deviation of the strains is very high (2144 $\mu\epsilon$) due to these distortions. To cope with them, a built-in correction method in Vic2D using rigid body translations was performed on the images, and the correlation is performed again. The results are shown in Figure 4.6.

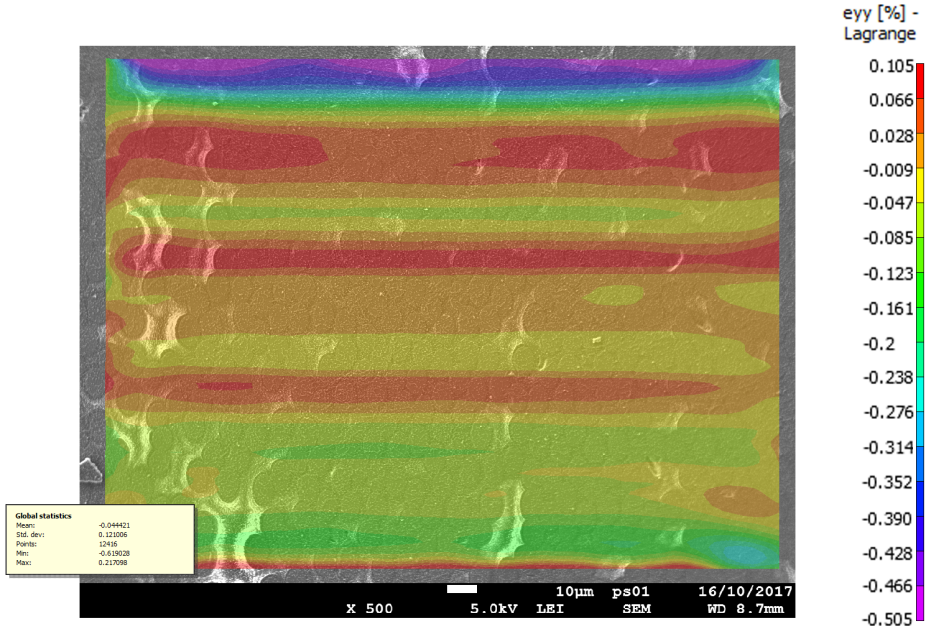

Figure 4.6: Strain in y-direction when DIC is applied on the SEM images, with correction.

After the correction is performed, the influence of the distortions is still present. However, it is less, which is also reflected in the standard deviation of the strain, which dropped to 1210 $\mu\epsilon$. Besides the distortions, there is also another source of error visible in both images, which is due to the charging. At spots where charging is present, the matrix-rich regions which are whiter in the image due to the lesser conductivity, the calculated strain deviates from the pattern.

4.1.5. Conclusion

Preliminary tests did not show rigid body motion DIC results accurate enough to continue and add a loading device to the system. The optical and SEM both did not show good results, but the SEM showed intricate distortion patterns due to the image creation method inherent to the SEM, which is hard to correct for [28]. Therefore, it is chosen to continue with the Keyence optical digital microscope. Since at the highest magnification (2500x), the pixel resolution is 86 nm, well under the optical resolution, the magnification is set to 2000x. This increases the FOV to 170 µm by 129 µm, more than enough to compare with a RVE simulation. The pixel resolution goes to 106 nm, still well below the optical limit. In Section 4.2, different causes for the error in optical microscopy are examined and improvements are suggested.

4.2. System characterization and improvement

After baseline tests are performed in Section 4.1, different phenomena have been identified which can influence the DIC results . The three most important error sources are vibrations, distortions and optical resolution limit. This results in a conclusion on how the best results can be achieved.

4.2.1. Vibrations

Preliminary investigation

To perform a quick check to indicate whether there is some influence of vibrations on the DIC errors, a simple experiment was performed. Series of 100 static images are taken in 3 different conditions: during daytime, during the evening and with the monitor of the Keyence on a separate table. The assumption is made that during the evening, there are less vibrations in the lab, because no one is walking around or performing other experiments in the building. The monitor of the Keyence is removed because this could be a source of vibration as well. The error in the DIC measurements is defined as the average (over the 100 stationary images) of the standard deviation of the strain in x-direction. More information about this quantification is found in Section 1.5. DIC parameters used for processing the images with Vic2D are: subset size of 29 pixels, step size of 11 pixels, strain filter of 15 subsets. The imaged specimen is a carbon fiber specimen speckled with 100 nm polystyrene spheres. Results are given in Table 4.2.

Table 4.2: Results of the preliminary vibration experiments

	Daytime	Evening	Monitor apart
Average of $\sigma(\epsilon_{xx})$	923 $\mu\epsilon$	768 $\mu\epsilon$	390 $\mu\epsilon$

From these results can be concluded that there is an influence of vibrations on the DIC errors, because the error is less in the evening. When placing the monitor of the Keyence apart on another table, the error drops significantly. This is an indication that this monitor is possible an important source of vibrations leading to errors.

Vibration measurements
Now that is determined that vibrations influence the results, the vibrations are measured. For this, the Keyence microscope is transferred to another lab equipped with a Polytec PSV-500 Scanning Vibrometer, shown in Figure 4.7. Using the Doppler shift from the reflected laser beams, the frequency and amplitude of vibrations can be determined. The vibrations of the microscope lens are measured. In fact, the relative movements/vibrations between specimen and lens are of interest, but it is assumed that they are of equal order of magnitude, with the lens having slightly larger movement due to the geometry of it. Hence, only the lens vibrations are measured. In two conditions, images are made while vibrations are measured. The conditions are with the monitor of the Keyence next to the stage, and again with the monitor on a separate table. Again, when processing 100 stationary images with the same DIC parameters as before, placing the Keyence monitor apart gives an improvement. In this particular setup, the error (average of standard deviation of strain in x-direction) goes from 1081 $\mu\varepsilon$ to 648 $\mu\varepsilon$ when removing the monitor. Note that these values are higher than before, which is because the table where the Keyence is put on is different and probably worse, since it is a simple wooden table instead of a heavy marble table. In Figure 4.8, the vibration spectra of the 2 conditions are presented in a graph. Vibrations are measured from 0 to 800 Hz, but no notable vibrations above 60 Hz are present. Measurements are made during 60 seconds, over which the vibrations are averaged.

Figure 4.7: The Polytec PSV-500 Scanning Vibrometer [26].

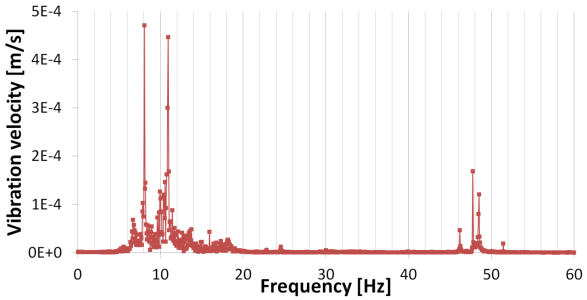

(a) The vibration spectrum with the monitor next to the stage and lens.

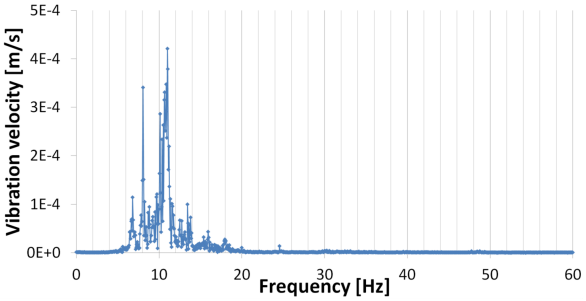

(b) The vibration spectrum with the monitor on a separate table.

Figure 4.8: Vibration spectra of different setups.

From this graph can be noted that there are, in both cases, notable vibrations in the 5-20 Hz range. Between the graphs is a difference; when the monitor is next to the stage, a vibration around 50 Hz is observed. This is the vibration caused by the monitor. The other vibrations are inherent to the building, and are not that easily eliminated. As the shutter time of the camera is 250 Hz, a vibration of 50 Hz can have an important influence on the image.

Actively damped table experiments
To further eliminate vibrations, the Keyence was moved to a an actively damped table, with the monitor on a separate table.

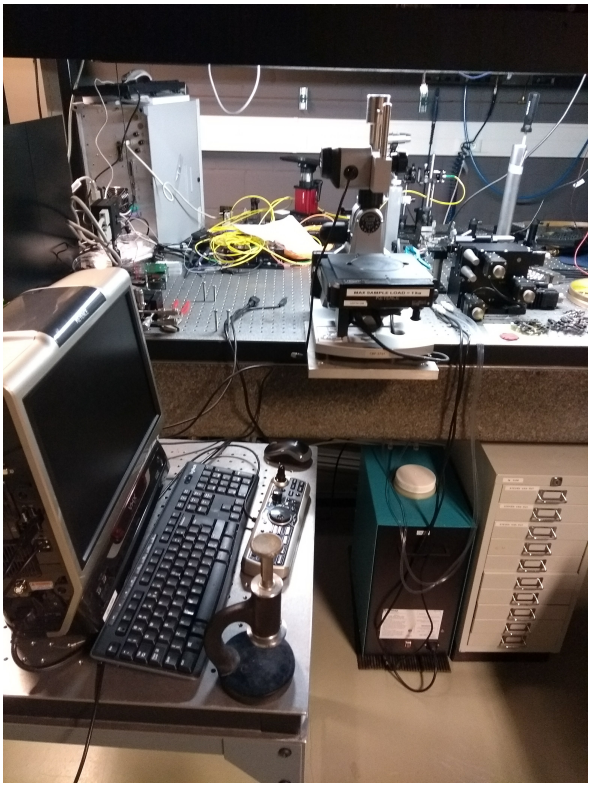

(a) The setup of the Keyence with monitor apart.

(b) A close-up of the damping system.

Figure 4.9: The actively damped setup at the CMST (Ghent University) lab.

Table 4.3: Correlation results of the images from the actively damped setup.

	Polystyrene spheres		
	100 nm	500 nm	1 µm
CF; average of $\sigma(\epsilon_{xx})$	378 $\mu\epsilon$	395 $\mu\epsilon$	1462 $\mu\epsilon$
GF; average of $\sigma(\epsilon_{xx})$	992 $\mu\epsilon$	3166 $\mu\epsilon$	2754 $\mu\epsilon$

Using this setup, again 100 images per sample are made to run the DIC algorithm on, with again the same parameters (subset size of 29 pixels, step size of 11 pixels, strain filter of 15 subsets). The results (average of standard deviation of strain in x-direction) of the images series of different specimens are listed in Table 4.3.

These results show that, for this given subset size, the 100 and 500 nm polystyrene spheres work best, especially on the CF. However, if the results are compared to the results from the preliminary test in Table 4.2, where CF was speckled with 100 nm polystyrene spheres, the result is only marginally better (378 $\mu\epsilon$ instead of 390 $\mu\epsilon$). From this, the conclusion is drawn that isolating the monitor of the Keyence from the stage is sufficient.

4.2.2. Distortion

Model

In the distortion model used, 2 major distortion types are included. These are the radial and tangential distortion [36]. The radial distortion is a result of lens imperfections, and the tangential distortion occurs when the imaging plane us not exactly parallel to the lens [22]. Radial distortion is corrected by Equation 4.1, and the tangential by Equation 4.2.

$$x_{corrected} = x(1 + k_1 r^2 + k_2 r^4 + k_3 r^6) y_{corrected} = y(1 + k_1 r^2 + k_2 r^4 + k_3 r^6) \tag{4.1}$$

$$x_{corrected} = x + [2p_1 xy + p_2(r^2 + 2x^2)] y_{corrected} = y + [p_1(r^2 + 2y^2) + 2p_2 xy] \tag{4.2}$$

With these equations, the distortion is determined by 5 parameters, the distortion coefficients (k_1 k_2 p_1 p_2 k_3).

Calibration & Correction

To determine the distortion parameters of the system, a calibration has to be performed. For this, a calibration pattern with traceable features is needed. These features have to be known with high precision, as the known position will be compared to the measured position in a non-linear optimization to find the best fitting distortion parameters [28]. Two different kinds of features have been used extensively, a chessboard pattern (for corner tracking) or a circular grid (for ellipse center tracking). It is important to design a calibration pattern with enough features covering the whole FOV. As the size of it is 170 µm by 128 µm with the Keyence on magnification 2000x, recognizable features (chessboard crossings or circle centers) are placed 10 µm apart. Designs are shown in Figure 4.10. In Figure 4.10a can be seen that only the edges of the black squares of the chessboard are drawn. As the location of corners of the chessboard are determined with an edge detection, this is sufficient while decreasing the production time drastically. This resulted in a new, self-made design that is usable while also manufacturable.

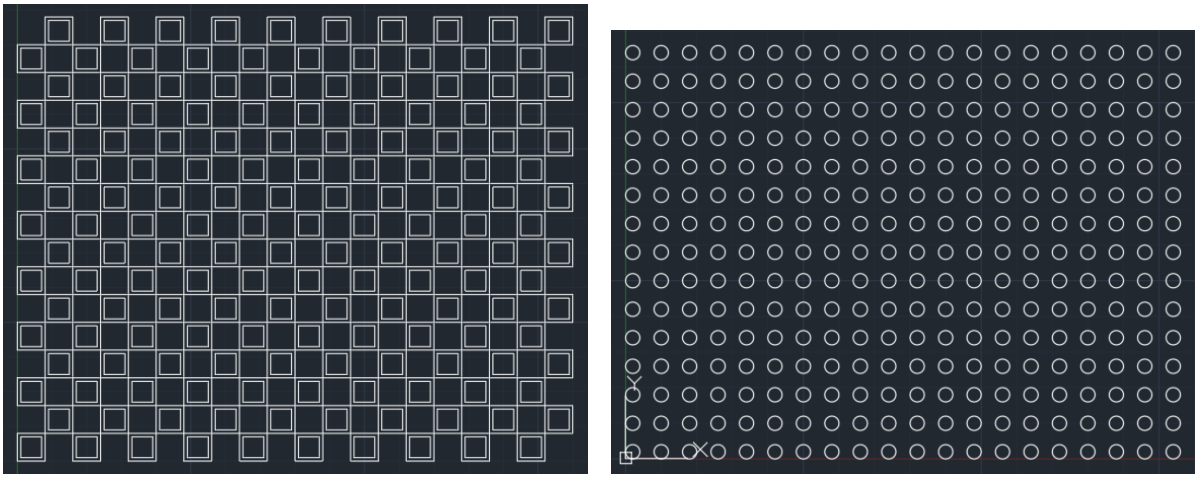

(a) Drawing of the circular grid.

(b) Drawing of the chessboard.

Figure 4.10: Computer aided design drawings of the calibration patterns, made with Autocad.

As these calibration patterns are very small, and high accuracy is needed to find the distortion parameters, the pattern is made with e-beam lithography. This was done at NaMiFab (Ghent University), the expertise center for Nano- and Microfabrication. Production process is as follows:

1. Cleaving 20x20 mm square from Silicon wafer
2. Cleaning with Acetone/IPA/DI-water
3. Oxygen plasma treatment Tepla, 12 min
4. Spincoating the resist
    - Positive e-beamresist ARP-6200.09 (SCAR62)
    - Spin recipe: 4000rpm, 500acc, 1min (gives 200nm thickness)
    - Bake at 150°Cfor 1 min on hotplate
5. E-beam lithography with Voyager (Raith)
    - 30 kV - mode LC60um
    - Dose sweep 3x3 (1,1-1,5uC)
    - Import computer aided design - calibration patterns.csf
    - Area dose - step size 0.010
    - Develop 1min n-amylacetate 99% + stopper 30" IPA

With this method, an accuracy of 10 nm is claimed to be achieved by the NaMiFab expertise center. An overall view of the calibration pattern is given in Figure 4.11.

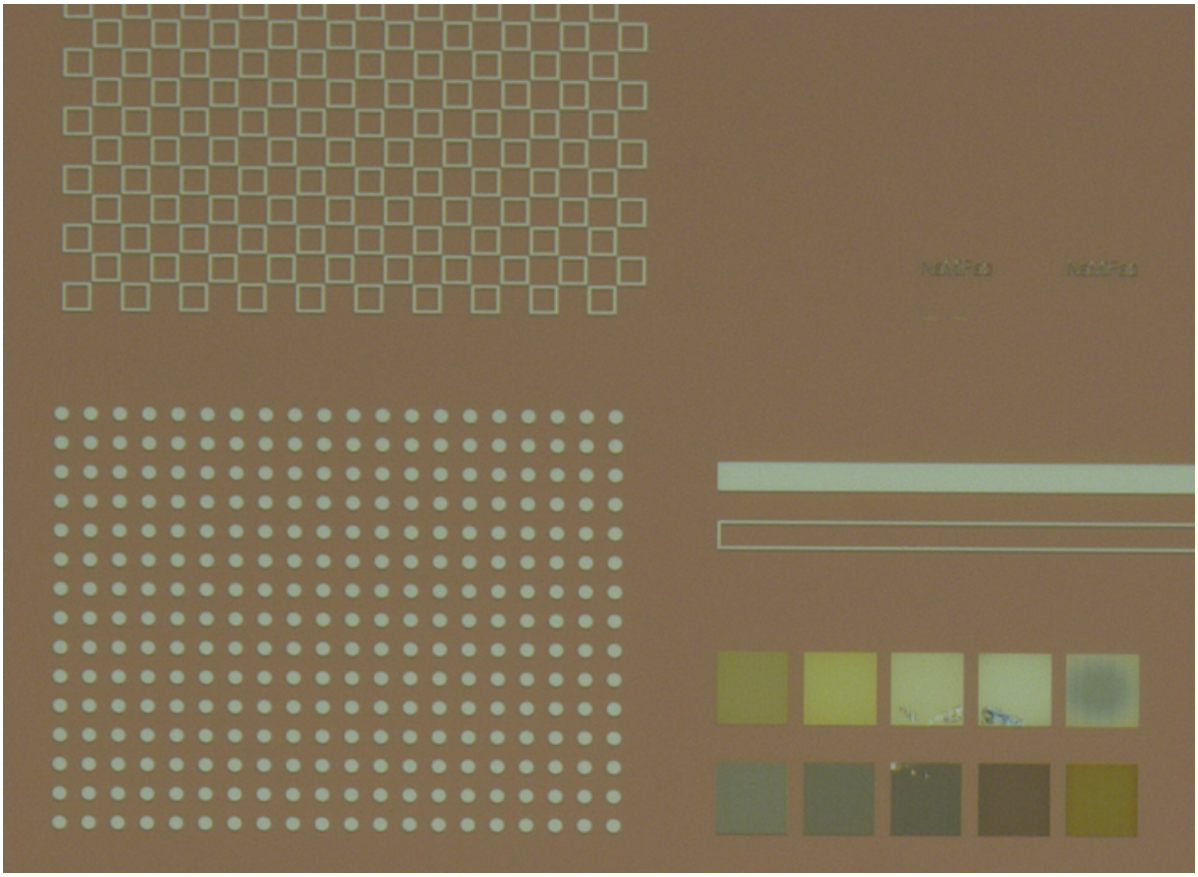

Figure 4.11: Overall view of the calibration pattern (magnification 1000x).

Images of the calibration patterns are made and OpenCV [22] is used to detect the features and to calculate the distortion parameters and maps. To do so, a Python script is written, with which the calibration is performed. The script is added in Appendix A. The location of the features is shown in Figures 4.12 and 4.13. At this zoom level, edges are not perfectly sharp. For the detection of circles, this is not a problem, but for the detection of the chessboard corners it is. This is because this method relies on edge detection. In the close-up of the recognized chessboard calibration image in Figure 4.12b, this is clearly visible, as the blue line connecting the edges is jagged instead of straight. In the images of the circular grid, this phenomena was not visible. As such, the circular grid was demonstrated to be better and is used further.

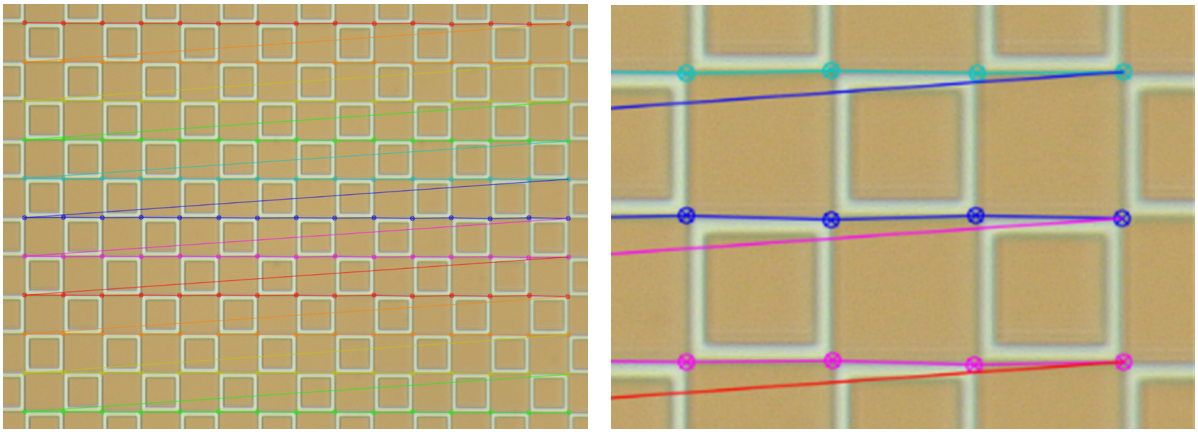

(a) Recognized calibration image of the chessboard pattern (magnification 2000x).

(b) Close-up of the recognized calibration image.

Figure 4.12: The chessboard calibration image, with recognized corners.

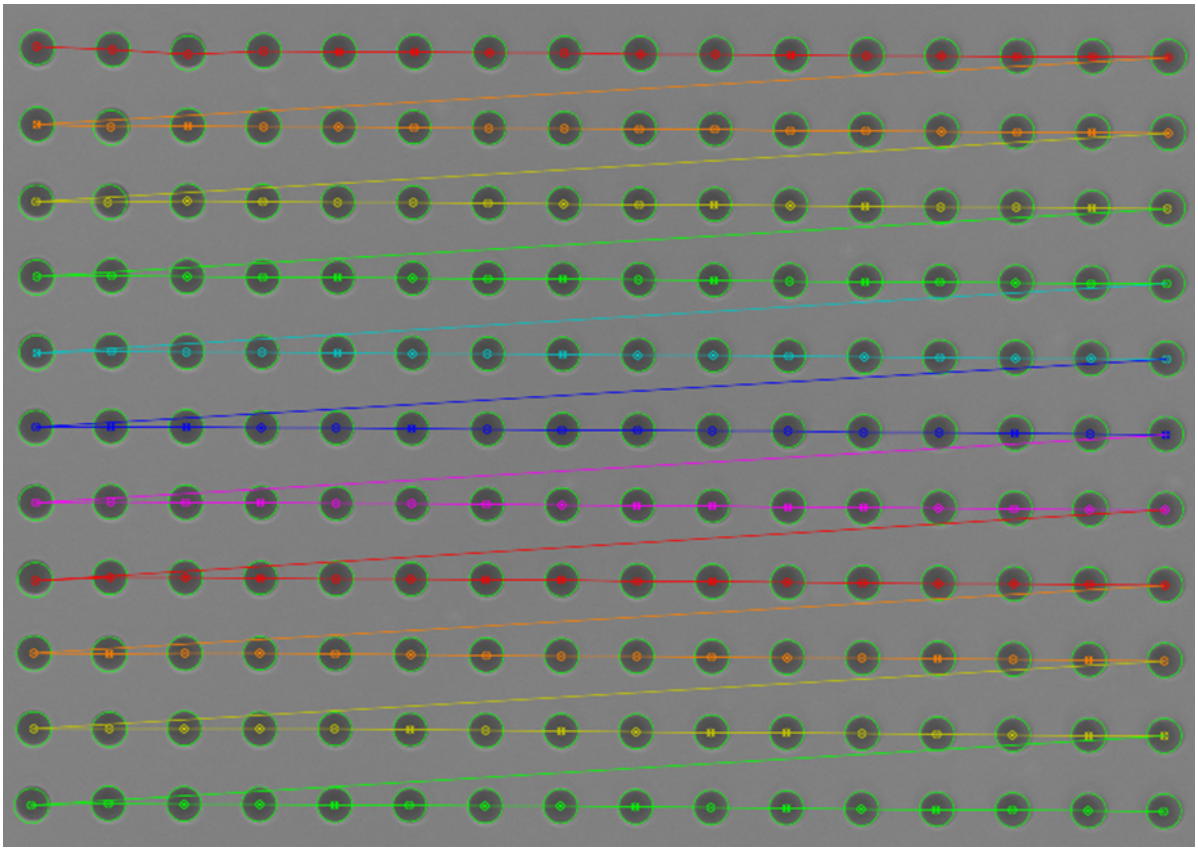

Figure 4.13: Recognized calibration image of the circular grid, inverted for feature detection (magnification 2000x).

With a series of 20 images, the microscope can be calibrated, with the script from Appendix A that determines the distortion parameters from these images [22]. Based on these parameters, distortion maps are created, as shown in Figure 4.15. Example values of distortion parameters are shown in Table 4.4.

Table 4.4: Distortion parameters

Distortion parameter	k_1	k_2	p_1	p_2	k_3
Value	5.49	-0.322e-1	0.0675	0.0135	0.000162

The radial and tangential distortions are also compared to each other, in Figure 4.14. The maximum of the radial distortion (Figure 4.14a) is 1.35 pixels, and only occurs in the corners of the FOV. More to the center of the image, the maximum is 0.75 pixel. The maximum of the tangential distortion is 2.7 pixels, and occurs in the center region of the image. As such, tangential distortion plays a bigger role, although this was not clear from the coefficients alone. As mentioned before, tangential distortion is due to a misalignment between lens and imaging plane. The reason for this is most probably the connection between the lens system and the camera of the Keyence. Since this is removable, it can wear out after time. Care has to be taken that this is tightened properly before calibration, and that is is not touched afterwards.

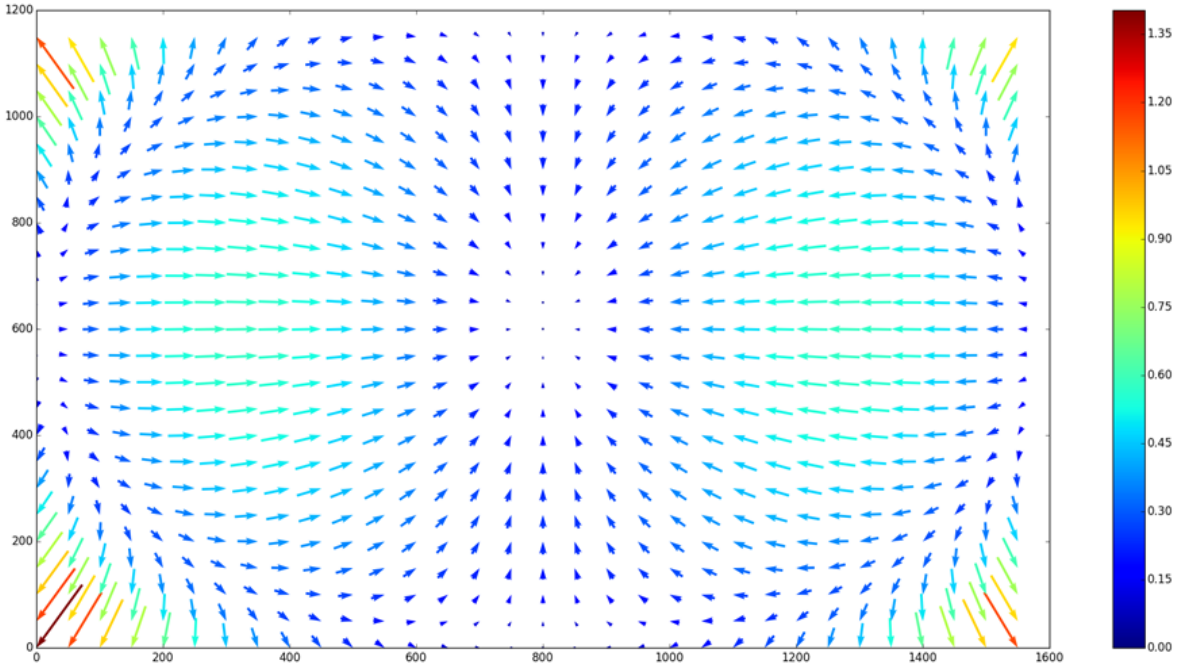

(a) The radial distortion component plotted. All units are pixels, either position or distortion displacement.

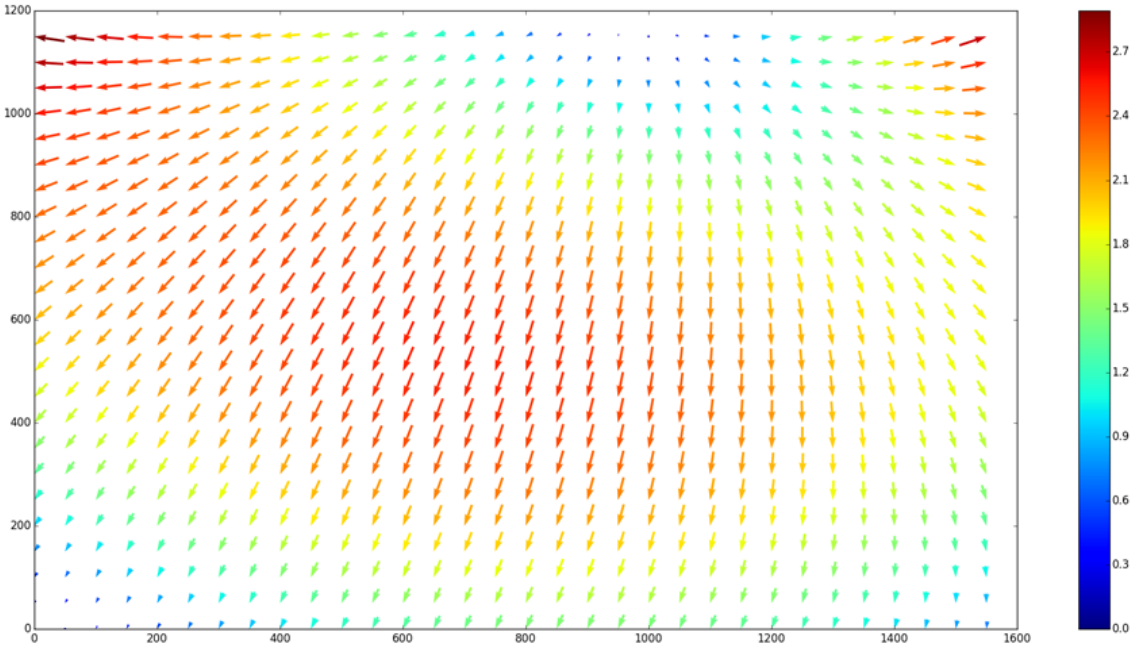

(b) The tangential distortion component plotted. All units are pixels, either position or distortion displacement.

Figure 4.14: Comparison of radial and tangential distortion.

Furthermore, from Figure 4.15, an important conclusion can be drawn. In Figure 4.15a, two distortion maps are plotted, and between these two, the Keyence VH-Z250R/W was removed and put back in place. The distortion maps are different, which indicates that calibration has to be performed every time the system is changed. Contrary, in Figure 4.15b, 3 distortion maps are plotted, when in between refocusing happened. These distortion maps show little difference (the 3rd map is even not visible since it is fully covered by the other arrows). This is important, because it shows that the distortion parameters do not depend on the focus. Therefore, distortion parameters can be determined for the system with the calibration pattern, and then can be focused on the specimen of interest.

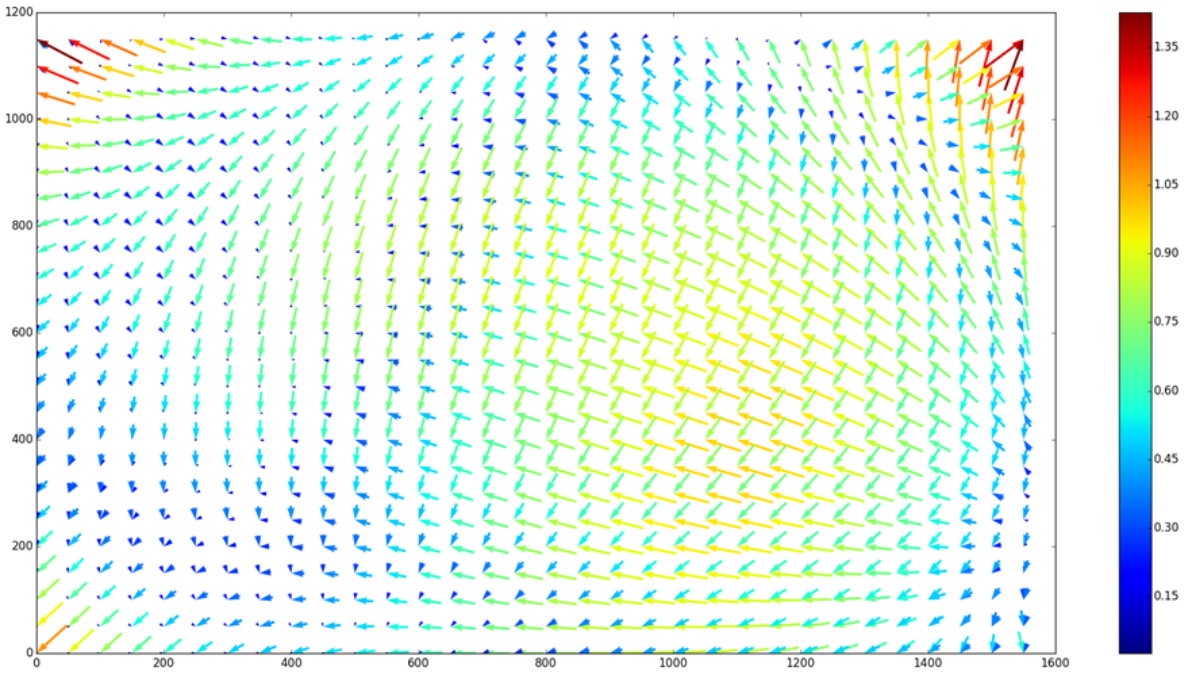

(a) Overlay of distortion maps, when the lens changed in between the creation of calibration image series. All units are pixels, either position or distortion displacement.

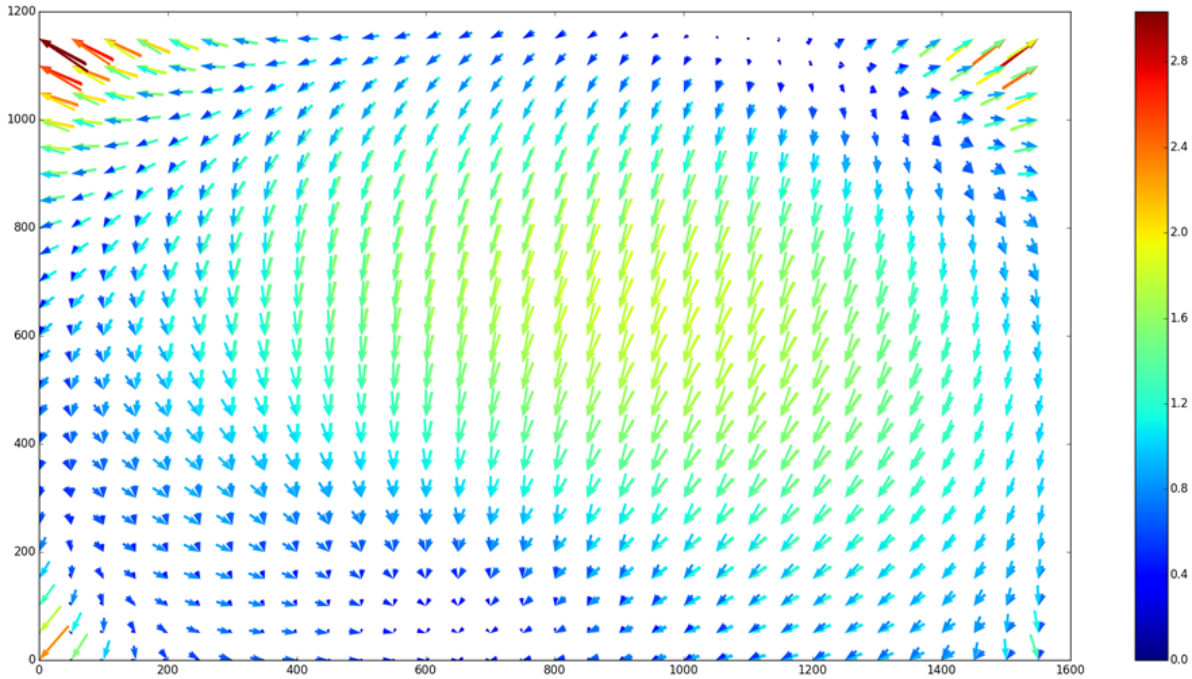

(b) Overlay of distortion maps, when refocusing happen between the creation of calibration image series. All units are pixels, either position or distortion displacement.

Figure 4.15: Comparison of distortion map under different conditions.

Table 4.5: Average standard deviations of strains in x-direction, comparison between original images and images corrected for distortion.

		Polystyrene spheres		
		100 nm	500 nm	1 µm
CF	Original	378 $\mu\epsilon$	395 $\mu\epsilon$	1462 $\mu\epsilon$
	Corrected	413 $\mu\epsilon$	395 $\mu\epsilon$	1549 $\mu\epsilon$
GF	Original	992 $\mu\epsilon$	3166 $\mu\epsilon$	2754 $\mu\epsilon$
	Corrected	832 $\mu\epsilon$	2774 $\mu\epsilon$	1903 $\mu\epsilon$

Results
When the distortions are known, distorted images are remapped, using linear interpolation between pixels. The influence on the DIC results is summarized in Table 4.5. The results do not improve for every specimen, and on average the improvement in only 7%. This does not mean that distortion correction is useless. Due to the fact that stationary images are taken, no movement (except for the minimalized vibrations) are present. Without movement, every subset will undergo the sample displacement due to the distortion every time, and this way distortion effects are not pronounced during stationary tests. When motion or displacement occurs, it is important to perform the distortion calibration and correction.

4.2.3. Optical limit

As explained in the Literature Study [28], the resolution of optical microscopes is limited by the diffraction of light. The actual resolution Z of an optical microscope depends on the wavelength λ of the light used and the quality of the optical system, indicated by the Numerical Aperture (NA). This relation is given by the Rayleigh criterion in Equation 4.3 [29]. Digital microscopes creating images with greater pixel resolution than the optical one are oversampling the same information.

$$Z = \frac{0.61 * \lambda}{NA} \tag{4.3}$$

At 2000x magnification, the Keyence has a pixel resolution of 106 nm. However, such a high optical resolution is theoretically not possible, even with a perfect microscope ($NA = 1$). As the numerical aperture of the Keyence microscope is not disclosed by the manufacturer, the optical resolution has to be measured. A common practice to measure resolution is the use of Ronchi rulings. These are gratings of high contrast colored (mostly black and white) parallel lines. If the lines can be distinguished from each other in an image, the resolution according to the spacing of the lines is achieved. Therefor, Ronchi rulings are included in the calibration pattern used in Section 4.2.2, visible in the bottom left of Figure 4.11. The spacing between lines starts at 500 nm, and decreases in 50 nm steps to 50 nm. An image on the highest magnification (2500x) of the Keyence is displayed in Figure 4.16. The bottom left is the one with 500 nm spacing, and the spacing decreases to the right. On the top left, the one with 250 nm spacing is located, and to the right of it, the grating with 200 nm spacing. With this spacing, the lines are not distinguishable anymore. The optical resolution of the system is thus 250 nm. This means that single polystyrene spheres of 100 nm are not visible under the optical microscope. However, they still form a visible speckle pattern, because they cluster together, which is clearly visible on SEM images in Figure 3.14.

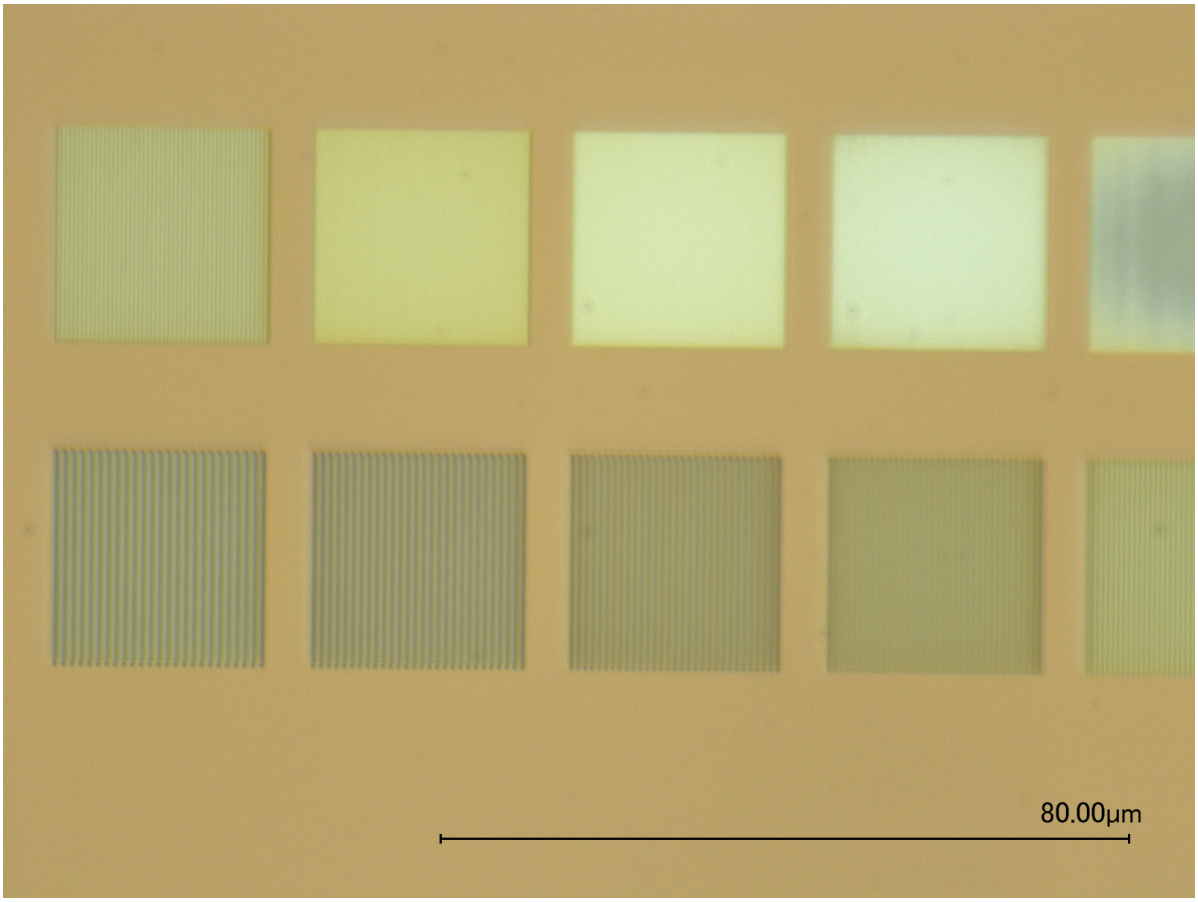

Figure 4.16: Microscopic image of the Ronchi rulings (magnification 2500x).

According to the Nyquist sampling theorem, the sampling frequency should be at least double of the frequency of the signal. Translating this to DIC means that every speckle should at least be two pixels in every direction. However, due to practical reasons such as noise in the camera and a finite gap between pixels, three pixels are required [7]. However, the amount of pixels is not the limit here, but the optical resolution. Gaps between pixels are thus not that relevant, but noise still is. Instead of an amount of pixels, to comply with the Nyquist sampling theorem, speckle features should be at least twice the optical resolution. This would result in a size of at least 500 nm. If the feature size is too small, aliasing will occur, introducing bias in the displacement estimates [36]. Therefor, Sutton et al. [36] even advise a feature size of 3 to 6 times the resolution (750 nm to 1.5 µm) to achieve good sampling. Regarding the subset size, they advise to have at least 3 features in every direction for reasonable accuracy. If the assumption is made that between speckles, there is the spacing of 1 speckle, subsets would need a size of 4.5 µm. This is 75% of the size of a carbon fiber, and larger than the wanted subsets in the project. Nevertheless, particles smaller than 500nm are also used, since clustering of them leads to features of larger size.

As during the project smaller subsets and speckles are used, this is a possible explanation of the errors in the measurements. When the 100 nm speckles are used, only clusters of them are visible. These clusters can provide a nice pattern, but still single spheres and very small clusters of a few spheres are present on the surface (see Figure 3.14a and 3.14b). These lead to aliasing, and thus to errors. At the other hand, using larger particles leads to not having enough particles in the desired subsets, also leading to errors.

4.3. Conclusion

As imaging system, the Keyence VHX-2000 digital microscope, equipped with the Z250-R lens is preferred over the JEOL 7600F, as preliminary results showed less distortions in the optical system. At the highest magnification (2500x) of the Keyence, the pixel resolution is 86 nm, well under the optical resolution, so the magnification is set to 2000x. This increases the FOV to 170 µm by 129 µm, more than enough to compare with a RVE simulations. The pixel resolution goes to 106 nm, still well below the optical limit. This ensures that all possible information is captured.

From the experiments in Section 4.2, the following can be concluded. Regarding the vibrations, there is indeed an influence. The biggest source of vibrations is the monitor of the Keyence digital microscope itself. As such, this should be isolated from the optical part of the setup (stage, lenses and camera). Distortions have been measured, and especially the tangential distortion is big. Distortions differ every time the lens is changed, so calibration has to be performed every time the system is set up. However, there is no distortion change due to refocusing, which makes the calibration actually useful because refocusing from the calibration target to a specimen is possible. Care has to be taken that the system components do not move, and especially the connection between camera and lens system seems to be fragile. To perform the calibration, a target with a circular grid is designed and produced using e-beam lithography. Taking a series of images of it and analyzing them with a Python script determines the calibration parameters. Lastly, the optical limit is a big problem. The optical resolution of the Keyence imaging system is only 250 nm. Taking into account 2 rules for good DIC accuracy, leads to a speckle feature size of at least 500 nm, preferably 750 nm to 1.5 µm. Subset size would be at least 4.5 µm. This is a big issue, since finer subsets are preferred for the project. Therefore, in Chapter 5, the influence of smaller subsets on the accuracy is determined.

5

DIC Algorithm

In this Chapter, the influence of the algorithm parameters on the displacement determination accuracy is determined. The most important parameter of the algorithm is the size of the subset, of which the influence is determined in Section 5.1. In Section 5.2, the influence of the shape is determined. As images, the images from optimal conditions are taken at magnification 2000x. These are images taken on the actively damped table, discussed in Chapter 4. From this setup, 20 static images are taken of each specimen to provide statistically relevant data.

5.1. Subset size

The most important DIC parameter is the size of the subset. Bigger subsets give more accurate results, as more speckles are captured in them. In this Section, the relation between accuracy and subset size is defined for each type of speckle. With six image series (2 materials, CF and GF and 3 sizes of nanoparticles) of 20 images, the DIC is performed by Vic2D with varying subset size. From the results, the accuracy is determined as described in Section 1.5. The results is summarized in the graph in Figure 5.1.

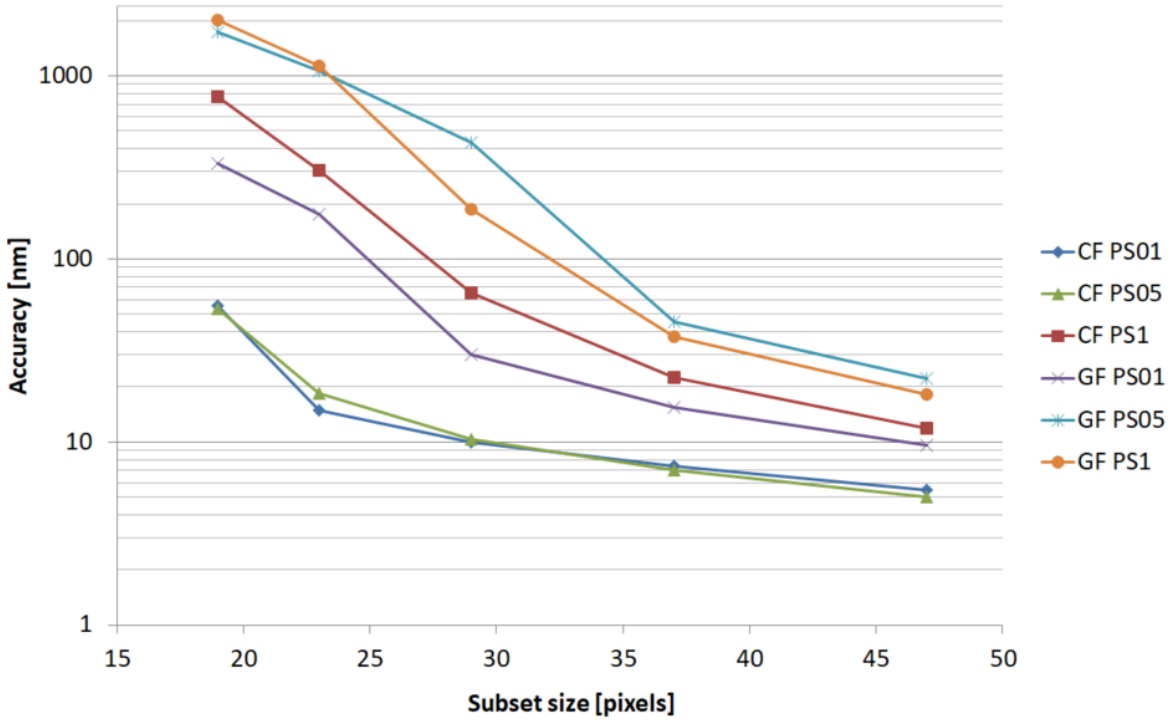

Figure 5.1: The influence of the subset size on the accuracy, for different substrates and nanoparticles.

In this graph, a clear correlation is seen between subset size and accuracy, which is logical [28]. Furthermore, the polystyrene spheres of 100 nm and 500 nm, on CF, perform best. Performance on GF is worse, probably because the distribution of the speckles on it was worse. There is thus still room for improvement of the speckling for GF, as in theory the same accuracy as on CF could be achieved. The accuracy requirement of 10 nm is satisfied on CF with the 2 smallest nanoparticles from subset size 29 pixels or bigger. For GF, it is only met from a size of 47 pixels. At the current magnification, these sizes correspond to 3.1 µm (29 pixels) and 5.0 µm (47 pixels).

5.2. Subset shape

In most commercial DIC software packages, rectangular subsets are implemented. However, an open source 2D DIC implementation in MatLab, named Ncorr [3], uses circular subsets. Using this piece of software, the same series of images as in Section 5.1 is processed. The images for this comparison are those of the CF with 100 nm polystyrene spheres applied as speckle pattern. Results are summarized in Figure 5.2, and a comparison is made based on subset size and on subset area. This is done because a circular subsets have only $\frac{\pi}{4}$ of the area of a square subset for a given size. This gives the circular subsets less pixels (and thus information) to perform the correlation on.

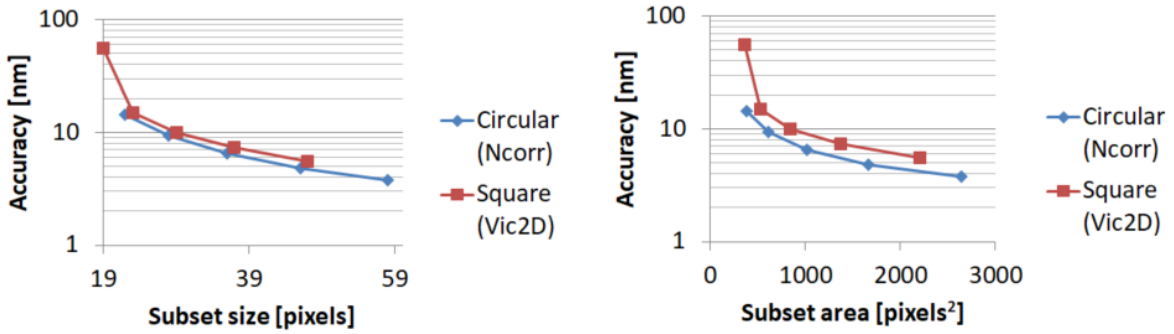

(a) Accuracy versus subset size.

(b) Accuracy versus subset area.

Figure 5.2: The influence of the subset shape on the accuracy.

From these graphs can be concluded that, the circular subsets perform, even when compared to size, slightly better than the square subsets. This means that the extra area in the corners of a square subset do not provide an advantage. Furthermore, this also means that, in this particular case, the open source algorithm performs a little bit better than the commercial one. The accuracy requirement of 10 nm is again satisfied with the square subset of 29 pixels, or the circular subsets with diameter 28 pixels.

5.3. Conclusion

From this chapter can be concluded that the size of a subset has a big influence on the accuracy of the results. To comply with the 10 nm accuracy criterion set up, subset size has to be at least 29 pixels for 100 or 500 nm polystyrene spheres on CF, and 47 pixels for GF with 100 nm polystyrene spheres. Regarding the shape of the subset, there is not a lot of influence. Circular subsets from open source software perform marginally better than the square subsets from a commercial software package. The fact that fibers are circular does not translate to a preference for either circular or square subsets.

6

Conclusion & Recommendations

In Section 6.1, an answer to the research questions set up in Section 1.2 is formulated, based on conclusions from the previous chapters. After that, recommendations for further research are listed in Section 6.2.

6.1. Conclusion

Regarding the preparation of the CF and GF composite specimens, unidirectional composites are first manufactured by infusion with epoxy resin. After curing, they are cut into pieces. After that, automatic polishing is performed with specific polishing sequences for each type of composite. To do this, the specimens are embedded in epoxy resin, but specially designed holders to clamp specimens could also be useful when a predetermined specimen shape is needed. Surface treatments with plasma is not beneficial, since it is shown that it has a negative influence on the surface.

To find a good speckling method, different methods are tried out. These are template patterning, using a magneto sputtering device and different masks, and nanoparticle patterning. To deposit the nanoparticles, different methods are evaluated. These are drop deposition, dip-coating, electrospraying and airbrushing. Two kinds of nanoparticles are evaluated, polystyrene microspheres (size 100 nm, 500 nm and 1 μm) and Aerosil fumed silica. Application of polystyrene microspheres with an airbrush proved better than the other methods, and this method is optimized. The most important parameter for this method is the amount of layers deposited. To quantify how good a speckle pattern is, the built-in match confidence of Vic2D is used. Depending on the size of the nanoparticle, an optimal amount of layers to create the speckle pattern is determined.

As imaging system, the Keyence VHX-2000 digital optical microscope with Z250 lens is chosen over the JEOL 7600F SEM. This is because the SEM showed intricate distortion patterns, which are hard to correct for. Furthermore, the FOV of the Keyence is 170 µm by 127 µm, which is large enough to provide meaningful results which can be compared with simulations. However, different issues are present when using this microscope for DIC. The first one is that vibrations have a strong influence on the results. Therefor, the imaging system should be isolated from the computer of the Keyence. Using an actively damped table did not provide significant improvement. A second issue is the distortion of the lens system. A microscale calibration pattern is developed to measure this distortions, split up in radial and tangential distortion. Especially the tangential distortion is big. Distortions differ every time the lens is changed, so calibration has to be performed every time the system is set up. However, there is no distortion change due to refocusing, which makes the calibration actually useful because refocusing from the calibration target to a specimen is possible. Care has to be taken that the system components do not move, and especially the connection between camera and lens system seems to be fragile. The last issue is the optical resolution of the system, which is measured to be 250 nm. This puts a limit on the size of usable nanoparticles, and the 100 nm particles are only visible when clustered, but are still very useful.

Concerning the influence of the algorithm on the results, it is known from literature that the size of a subset has significant influence on the accuracy [28]. The exact relation between subset size and accuracy is determined for the different materials and nanoparticle speckles. From this can be concluded that the 10 nm accuracy is possible on CF with a 29 pixel (3.074 µm) subset with either 100 nm or 500 nm nanoparticles applied on the surface. For GF, the 10 nm accuracy is achieved when a subset of 47 pixels (4.982 µm) is used in combination with the 100 nm polystyrene spheres. To determine the influence of the shape of subsets, the DIC is also performed with the open source software Ncorr [3], using circular subsets. These subsets provide, for equal subset size in comparison to the square subsets used by Vic2D, only a marginal improvement. The circular shape of a fiber does not translates to a preference for a certain shape of subset.

The final conclusion is that application of DIC on the microscale of composites is possible with an accuracy of 10 nm with this system described. The Keyence VHX-2000 provides calibrated, vibration-free images at 2000x magnification at an optical resolution of 250nm. Polished CF and GF specimens are speckled with nanoparticles of preferably 100 nm or 500 nm, deposited by an airbrush. An algorithm using either square or circular subsets can be used to process the images, and from a subset size of 29 pixels (3.074 µm), the accuracy of 10 nm is achieved for the CF specimens, whereas for GF the minimal subset size is 47 pixels (4.982 µm).

6.2. Recommendations

A first recommendation is regarding the limit of the optical resolution. Since this cannot be improved further due to physics, a switch to SEM can be made, providing better resolutions at the cost of more difficult distortion. Is this would be done, the speckling method presented in this thesis can still be used, as the speckles also provide good contrast in SEM. As shown in Chapter 5, subsets need at least to be 29 pixels, which is a rather poor spatial DIC resolution. With the imaging resolution of a SEM system being more than 100 times better, an increase in spatial DIC resolution can be possible. With the current spatial DIC resolution, RVE simulations are hard to validate. However, the Keyence optical system can still prove usefull, when for example larger length scales are studied (on ply level). Another interesting possibility is that during mechanical testing, debonding can be visible under the optical microscope. Doing just a visual assessment on when debonding starts is still very valuable information.

When mechanical testing is to be performed, care has to be taken that the whole FOV stays in focus during the testing. Refocusing can be possible, since this does not alter the distortions, but is not advised. What is even worse, are rotations of the surface, which cannot be countered by refocusing. The Poisson effect will play a large role here, since this cannot be eliminated. Due to this, there is an important difference between tensile testing and 3-point bending. With tensile testing, the Poisson effect will cause the specimen to contract perpendicular to the surface, since the tension is uniform. This is not the case for 3-point bending, where a rotation of the surface plane will take place due to tension at one side and compression at the other side of the specimen. Furthermore, it has been proven that vibrations have a bad influence on the DIC results. When loading is applied to specimens, care has to be taken that the loading device does noet introduce extra vibrations to the composite. Specimen preparation will also be different, since embedding the specimens will not be possible anymore. However, it is still possible to clamp specimens for automatic polishing. Care should be taken with the settings of the automatic polisher, since it exerts a certain force on the specimens. With a different area, a different pressure will thus be applied. Therefore, the applied force should be scaled with the area.

Bibliography

[1] J. D. Almer, A. A. T. Andonian, and S. N. Atluri. *Springer Handbook of Experimental Solid Mechanics*. 2008. ISBN 9780387268835.

[2] T. A. Berfield, J. K. Patel, R. G. Shimmin, P. V. Braun, J. Lambros, and N. R. Sottos. Micro- and nanoscale deformation measurement of surface and internal planes via digital image correlation. *Experimental Mechanics*, 47(1):51–62, 2007. ISSN 00144851. doi: 10.1007/s11340-006-0531-2.

[3] J. Blaber and A. Antoniou. Ncorr - Instruction Manual. 2015. URL `www.ncorr.com`.

[4] L. P. Canal, C. González, J. M. Molina-Aldareguía, J. Segurado, and J. Llorca. Application of digital image correlation at the microscale in fiber-reinforced composites. *Composites Part A: Applied Science and Manufacturing*, 43(10):1630–1638, 2012. ISSN 1359835X. doi: 10.1016/j.compositesa.2011.07.014. URL `http://dx.doi.org/10.1016/j.compositesa.2011.07.014`.

[5] Composites Manufacturing Magazine. State of the Composites Industry, 2016. URL `http://compositesmanufacturingmagazine.com/2016/01/state-of-the-composites-industry-lucintel-2016/`.

[6] F. Cougnon, K. Strijckmans, R. Schelfhout, and D. Depla. Hysteresis behavior during facing target magnetron sputtering. *SURFACE & COATINGS TECHNOLOGY*, 294:215–219, 2016. ISSN 0257-8972. URL `http://dx.doi.org/10.1016/j.surfcoat.2016.03.096`.

[7] J. Q. Da Fonseca, P. M. Mummery, and P. J. Withers. Full-field strain mapping by optical correlation of micrographs acquired during deformation. *Journal of Microscopy*, 218 (1):9–21, 2005. ISSN 00222720. doi: 10.1111/j.1365-2818.2005.01461.x.

[8] L. Daelemans. *Interlaminar toughening of composite laminates by electrospun nanofibrous interleaves*. PhD thesis, Ghent University, 2017.

[9] A. Guery, F. Latourte, F. Hild, and S. Roux. Characterization of SEM speckle pattern marking and imaging distortion by digital image correlation. *Measurement Science and Technology*, 25(1):015401, 2014. ISSN 0957-0233. doi: 10.1088/0957-0233/25/1/015401. URL `http://stacks.iop.org/0957-0233/25/i=1/a=015401?key=crossref.bbb7226ca8d60d98abfa6441c006b932`.

[10] T. Hobbiebrunken, M. Hojo, T. Adachi, C. De Jong, and B. Fiedler. Evaluation of interfacial strength in cf/epoxies using fem and in-situ experiments. *Composites Part A: Applied Science and Manufacturing*, 37(12):2248 – 2256, 2006. ISSN 1359-835X. doi: https://doi.org/10.1016/j.compositesa.2005.12.021. URL `http://www.sciencedirect.com/science/article/pii/S1359835X06000066`. The 11th US–Japan Conference on Composite Materials.

[11] T. C. Isabell and P. E. Fischione. Applications of Plasma Cleaning for Electron Microscopy of Semiconducting Materials. *MRS Proceedings*, 523:31, 1998. ISSN 1946-4274. doi: 10.1557/PROC-523-31. URL http://journals.cambridge.org/abstract{_}S1946427400181394.

[12] JEOL. Jsm-7600f, 2018. URL https://www.jeol.co.jp/en/products/detail/JSM-7600F.html. [Online; accessed February, 2018].

[13] A. D. Kammers and S. Daly. Small-scale patterning methods for digital image correlation under scanning electron microscopy. *Measurement Science and Technology*, 22(12):125501, 2011. ISSN 0957-0233. doi: 10.1088/0957-0233/22/12/125501. URL http://iopscience.iop.org/0957-0233/22/12/125501.

[14] A. D. Kammers and S. Daly. Digital Image Correlation under Scanning Electron Microscopy: Methodology and Validation. *Experimental Mechanics*, 53(9):1743–1761, 2013. ISSN 00144851. doi: 10.1007/s11340-013-9782-x.

[15] A. D. Kammers and S. Daly. Self-Assembled Nanoparticle Surface Patterning for Improved Digital Image Correlation in a Scanning Electron Microscope. *Experimental Mechanics*, 53(8):1333–1341, 2013. ISSN 00144851. doi: 10.1007/s11340-013-9734-5.

[16] H. J. K. Lemmen and R. C. Alderliesten. The power of Digital Image Correlation for detailed elastic-plastic strain measurements. *Emeseg*, pages 73–89, 2008. URL http://www.wseas.us/e-library/conferences/2008/crete/emeseg/emeseg09.pdf.

[17] Y. J. Li, H. M. Xie, Q. Luo, C. Z. Gu, Z. X. Hu, P. W. Chen, and Q. M. Zhang. Fabrication technique of micro/nano-scale speckle patterns with focused ion beam. *Science China Physics, Mechanics and Astronomy*, 55(6):1037–1044, 2012. ISSN 1674-7348. doi: 10.1007/s11433-012-4751-4. URL http://link.springer.com/10.1007/s11433-012-4751-4.

[18] G. Lionello and L. Cristofolini. A practical approach to optimizing the preparation of speckle patterns for digital-image correlation. *Measurement Science and Technology*, 25(10):107001, 2014. ISSN 0957-0233. doi: 10.1088/0957-0233/25/10/107001. URL http://iopscience.iop.org/0957-0233/25/10/107001/article/.

[19] B. D. Lucas and T. Kanade. An iterative image registration technique with application to stereo vision. *Proceedings DARPA Image Understanding Workshop*, pages 121–130, 1981.

[20] M. Mehdikhani, M. Aravand, B. Sabuncuoglu, M. G. Callens, S. V. Lomov, and L. Gorbatikh. Full-field strain measurements at the micro-scale in fiber-reinforced composites using digital image correlation. *Composite Structures*, 140:192–201, 2016. ISSN 02638223. doi: 10.1016/j.compstruct.2015.12.020. URL http://dx.doi.org/10.1016/j.compstruct.2015.12.020.

[21] M. Mehdikhani, A. Matveeva, M. A. Aravand, B. L. Wardle, S. V. Lomov, and L. Gorbatikh. Strain mapping at the micro-scale in hierarchical polymer composites with aligned carbon nanotube grafted fibers. *Composites Science and Technology*, 137:24–34, 2016. ISSN 02663538. doi: 10.1016/j.compscitech.2016.10.021. URL http://dx.doi.org/10.1016/j.compscitech.2016.10.021.

[22] Alexander Mordvintsev and Abid K. OpenCV Documentation - Camera Calibration. URL http://opencv-python-tutroals.readthedocs.io/en/latest/py{_}tutorials/py{_}calib3d/py{_}calibration/py{_}calibration.html.

[23] B. Pan, K. Qian, H. Xie, and A. Asundi. Two-dimensional digital image correlation for in-plane displacement and strain measurement: a review. *Measurement Science and Technology*, 20(6):062001, 2009. ISSN 0957-0233. doi: 10.1088/0957-0233/20/6/062001.

[24] B. Peuchot. Camera virtual equivalent model – 0.01 pixel detector. *Computerized Medical Imaging and Graphics*, 17:289–294, 1993.

[25] Polytec. Imagej, image processing and analysis in java, 2018. URL https://imagej.nih.gov/ij/. [Online; accessed June, 2018].

[26] Polytec. Psv-500 scanning vibrometer, 2018. URL https://www.polytec.com/eu/vibrometry/products/full-field-vibrometers/psv-500-3d-scanning-vibrometer/. [Online; accessed February, 2018].

[27] H. W. Schreier, J. R. Braasch, and M. A. Sutton. Systematic errors in digital image correlation caused by intensity interpolation. *Library*, 39(November):2915–2921, 2000.

[28] D. Schroyen. Application of Digital Image Correlation on the micro-scale of composites - Literature Study. Technical report, Delft University of Technology, 2017.

[29] W. J. Smith. *Modern Optical Engineering*. McGraw-Hill, New York, 3 edition, 2000. ISBN 0071363602.

[30] M. A. Sutton, W. J. Wolters, W. H. Peters, W. F. Ranson, and S. R. McNeill. Determination of displacements using an improved digital correlation method. *Image and Vision Computing*, 1(3):133–139, 1983. ISSN 02628856. doi: 10.1016/0262-8856(83)90064-1.

[31] M. A. Sutton, C. Mingqi, W. H. Peters, Y. J. Chao, and S. R. McNeill. Application of an optimized digital correlation method to planar deformation analysis. *Image and Vision Computing*, 4(3):143–150, 1986. ISSN 02628856. doi: 10.1016/0262-8856(86)90057-0.

[32] M. A. Sutton, T. L. Chae, J. L. Turner, and H. A. Bruck. Development of a computer vision methodology for the analysis of surface deformations in magnified images. *American Society for Testing and Materials*, pages 109–132, 1990.

[33] M. A. Sutton, N. Li, D. Garcia, N. Cornille, J. J. Orteu, S. R. Mcneill, H. W. Schreier, and X. Li. Metrology in a scanning electron microscope : theoretical developments and experimental validation. *Measurement Science and Technology*, 17:2613–2622, 2006. doi: 10.1088/0957-0233/17/10/012.

[34] M. A. Sutton, N. Li, D. Garcia, N. Cornille, J. J. Orteu, S. R. McNeill, H. W. Schreier, X. Li, and A. P. Reynolds. Scanning electron microscopy for quantitative small and large deformation measurements Part II: Experimental validation for magnifications from 200 to 10,000. *Experimental Mechanics*, 47(6):789–804, 2007. ISSN 00144851. doi: 10.1007/s11340-007-9041-0.

[35] M. A. Sutton, N. Li, D. C. Joy, A. P. Reynolds, and X. Li. Scanning electron microscopy for quantitative small and large deformation measurements Part I: SEM imaging at magnifications from 200 to 10,000. *Experimental Mechanics*, 47(6):775–787, 2007. ISSN 00144851. doi: 10.1007/s11340-007-9042-z.

[36] M. A. Sutton, J. J. Orteu, and H. W. Schreier. *Image Correlation for Shape, Motion and Deformation Measurements*, volume 53. 2009. ISBN 9788578110796. doi: 10.1017/CBO9781107415324.004.

[37] B. Winiarski, R. M. Langford, J. Tian, Y. Yokoyama, P. K. Liaw, and P. J. Withers. Mapping residual stress distributions at the micron scale in amorphous materials. *Metallurgical and Materials Transactions A: Physical Metallurgy and Materials Science*, 41(7):1743–1751, 2010. ISSN 10735623. doi: 10.1007/s11661-009-0127-4.

[38] S. Yaofeng and J. H. L. Pang. Study of optimal subset size in digital image correlation of speckle pattern images. *Optics and Lasers in Engineering*, 45(9):967–974, 2007. ISSN 01438166. doi: 10.1016/j.optlaseng.2007.01.012.

[39] R. Zhu, H. Xie, Y. Xue, L. Wang, and Y. J. Li. Fabrication of speckle patterns by focused ion beam deposition and its application to micro-scale residual stress measurement. *Measurement Science and Technology*, 26(9):095601, 2015. ISSN 0957-0233. doi: 10.1088/0957-0233/26/9/095601. URL `http://stacks.iop.org/0957-0233/26/i=9/a=095601?key=crossref.a70b9aa7dbb3b35fa05f6f656066aff5`.

A

Calibration script

```
# Standard imports
import cv2
import numpy as np
from matplotlib import pyplot as plt
import glob

#Load calibration images
images = glob.glob('calib_circ0000*.tif')

# Setup SimpleBlobDetector parameters.
params = cv2.SimpleBlobDetector_Params()

# Filter by Area.
params.filterByArea = True
params.minArea = 500

# Filter by Circularity
params.filterByCircularity = False
params.minCircularity = 0.9

# Filter by Convexity
params.filterByConvexity = False
params.minConvexity = 0.87

# Filter by Inertia
params.filterByInertia = False
params.minInertiaRatio = 0.01

# Create a detector with the parameters
ver = (cv2.__version__).split('.')
if int(ver[0]) < 3 :
    detector = cv2.SimpleBlobDetector(params)
```

```
else :
    detector = cv2.SimpleBlobDetector_create(params)

# termination criteria
criteria = (cv2.TERM_CRITERIA_EPS + cv2.TERM_CRITERIA_MAX_ITER, 30, 0.001)

# Original blob coordinates, supposing all blobs are of z-coordinates 0
points_x=16
points_y=11

objp = np.zeros((points_x*points_y,3), np.float32)
objp[:,:2] = np.mgrid[0:points_x,0:points_y].T.reshape(-1,2)

# Arrays to store object points and image points from all the images.
objpoints = [] # 3d point in real world space
imgpoints = [] # 2d points in image plane.

#Finding all circles in the calibration images
for fname in images:
    img = cv2.imread(fname, cv2.IMREAD_GRAYSCALE)
    iminv = cv2.bitwise_not(img)
    keypoints = detector.detect(iminv)
    im_with_keypoints = cv2.drawKeypoints(iminv, keypoints, np.array([]),
    \\ (0,255,0), cv2.DRAW_MATCHES_FLAGS_DRAW_RICH_KEYPOINTS)
    im_with_keypoints_gray = cv2.cvtColor(im_with_keypoints, cv2.COLOR_BGR2GRAY)
    # Find the ccenters
    ret, corners = cv2.findCirclesGrid(im_with_keypoints, (points_x,points_y),
    \\ flags=cv2.CALIB_CB_SYMMETRIC_GRID, blobDetector=detector)
    print ret
    # If found, add object points, image points (after refining them)
    if ret == True:
        objpoints.append(objp)
        corners2 = cv2.cornerSubPix(im_with_keypoints_gray,
        \\ corners,(11,11),(-1,-1),criteria)
        imgpoints.append(corners2)

#Determing calibration parameters
ret, mtx, dist, rvecs, tvecs = cv2.calibrateCamera(objpoints, imgpoints,
\\ img.shape[::-1],None,None)

h,  w = img.shape[:2]
newcameramtx, roi=cv2.getOptimalNewCameraMatrix(mtx,dist,(w,h),1,(w,h))
mapx,mapy = cv2.initUndistortRectifyMap(mtx,dist,None,newcameramtx,(w,h),5)

undistort=True
if undistort:
```

```
    for fname in images:

        img = cv2.imread(fname)
        # undistort

        dst = cv2.remap(img,mapx,mapy,cv2.INTER_LINEAR)

        # crop the image
        x,y,w,h = roi
        dst = dst[y:y+h, x:x+w]
        cv2.imwrite(fname[:-4]+'_undistorted.png',dst)

x=np.arange(0,w,dtype=np.float)
y=np.arange(0,h,dtype=np.float)
mapx_ideal, mapy_ideal = np.meshgrid(x,y)
diff_x=mapx-mapx_ideal
diff_y=mapy-mapy_ideal
#imgplot = plt.imshow(diff_y)
#plt.colorbar()
step=50
M = np.hypot(diff_x, diff_y)
Q=plt.quiver(mapx_ideal[::step, ::step], mapy_ideal[::step, ::step],
\\ diff_x[::step, ::step], diff_y[::step, ::step], M[::step, ::step], pivot='tip')
cb = plt.colorbar(Q)
```